Evaluation of Methods for Determining the Yoshida-Uemori Combined Isotropic/Kinematic Hardening Model Parameters from Tension-Compression Tests of Advanced Lightweighting Materials

Dilip K. Banerjee, William E. Luecke, Mark A. Iadicola, and Evan Rust
Material Measurement Laboratory
National Institute of Standards and Technology
Gaithersburg, MD 20899, USA

Abstract

The performance of two methods, termed Manual and Optimization, for determining the values of the constitutive-model parameters for Yoshida-Uemori (Y-U) isotropic-kinematic hardening model was evaluated. The Y-U parameters were determined for two 6000-series aluminum alloys (AA6XXX-T4 and AA6XXX-T81) and two dual-phase steels (DP 980 and DP 1180) using stress-strain data from tension and tension-compression tests. In the Manual Method the parameters were calculated by sequentially fitting the forward and then the reverse segments of tension-compression stress-strain data. In the Optimization Method, the parameters were calculated by systematically reducing the difference between the data and stress-strain curves computed from a one-element finite element model coupled with the optimization module of the commercial finite-element software package.

The performance of the methods was evaluated qualitatively by graphically comparing measured and computed stress-strain curves and quantitatively by evaluating the residual between the measured and computed curves. Although the quality of agreement for the Manual Method was generally good for the aluminum alloy tests, the agreement was inferior for the dual-phase steel tests, especially for the reverse deformation segment. The Optimization Method produced the best results as evaluated by the lowest residual between the measured and computed curves. Of several variants of the Optimization Method, simultaneous optimization against all three replicate curves produced Y-U parameters that best represented the measured stress-strain curves. Statistical analyses conducted in conjunction with optimization studies also established the relative influence for each of the Y-U parameters on the overall agreement between measured and computed curves.

A broader implication is that using a finite element model, rather than the manual methods, should be used to determine the Y-U parameters, since those parameters will be eventually used in a finite element model to simulate a forming process. This is especially true when determining a single set of parameters for repeat tests.

Keywords

Tension-compression test; Kinematic hardening; Yoshida-Uemori model; lightweighting material; finite element modeling; parameter optimization.

1. Introduction

As automotive industries are adopting advanced lightweight alloys for sheet metal components, it is becoming more important to predict accurately the mechanical behavior of these alloys during forming operations. One major challenge associated with the forming of advanced lightweight materials (e.g., advanced high-strength steels or AHSS) is the springback effect, which occurs during shaping and forming operations. Advanced alloys tend to show more springback, which is attributed to the Bauschinger effect [1]. Predicting and compensating for springback effects have been extensively studied by die makers [2,3]. A sufficiently robust constitutive model must be selected that can capture the material behavior throughout the intended forming operations. Such a model can be incorporated in a numerical model such as a finite-element analysis (FEA) model. For advanced alloys, accurate constitutive models, in addition to proper description of tool and binder geometries and contact conditions, are keys to developing a robust numerical model for studying forming of these materials. Constitutive models include both isotropic (i.e., expansion of the yield surface is uniform in all directions in stress space) and kinematic (i.e., the yield surface translates in stress space, rather than expanding) hardening models. Consequently, demand for accurate constitutive models that combine both isotropic and kinematic hardening and the data necessary for their calibration is increasing, because such models can predict the elastic recovery, residual stresses, and associated springback necessary to model complex loading behavior around draw-beads during forming operations.

Finite-element analysis software for modeling deformation has made it possible to use ever more sophisticated and realistic multi-parameter material models. Determining the optimum values of the many parameters for a proper constitutive model has progressed from using literature values and simple manual determinations [4–8] to simultaneous optimization for some or all of the parameters [8–22]. Some researchers have used custom code to compute a stress-strain curves for the material and a custom optimizer [13,23–25], or used a commercial closed-source package [22] to determine the parameters. Because the goal is almost always to eventually use the material model in a finite-element model of a more complicated forming operation, it is increasingly common to use the FEA solver to generate the stress-strain curve from the model, and then use either a commercial optimizer coupled to the FEA package [8,10–12,14,14–16,18–21] or a custom-written optimizer [9,26] to fine tune the parameter values based on comparing model data with test results. This optimization approach simplifies the determination of the values of the parameters by freeing the user from writing an implementation of the model separately.

Most of these articles focused on determining a set of material model parameters from a set of tension, tension-compression [8–11,13,15,17,19,20,22], bending [12,21,27], load-unload [4,9,10,12,16,20,27], or other [12,21,27] tests to use later in modeling a more complex forming operation. Comparatively little attention [14,19] has been devoted to quantitatively assessing the quality of the fit of the model parameters to the input stress-strain curves or their sensitivity [15] to the material model. Instead, because of the complexity of the material models, the evaluation of the quality of fit has been primarily visual and qualitative.

The Yoshida-Uemori (Y-U) work-hardening model [28,29] extends previous work-hardening models [30–42]. It has been widely used for modeling complex sheet-metal forming operations [10–12,14–16,18–20,22,27,43,44], especially those where springback or reverse deformation is important. It properly describes several important phenomena in sheet metal forming such as the transient Bauschinger effect, permanent softening, strain-range dependent cyclic hardening, and work-hardening stagnation in several steel grades. The Yoshida-Uemori model, described in much greater detail in the appendix, uses ten parameters, summarized in Table 1, to describe the evolution of the yield and bounding surfaces during both forward and reverse deformation processes. Because of its utility, at least three [45–47] major commercial software packages used for simulating sheet-metal forming have implemented this model to free users from developing custom implementation of the Y-U model in finite element codes using user subroutines. One such software package [45] has been used in this study. Constitutive models should comprise a combination of isotropic hardening, kinematic hardening, rotational hardening, and distortional (anisotropic) hardening models. For example, the homogeneous anisotropic hardening (HAH) framework[48] includes a combination of isotropic and distortional hardening and can be especially relevant for aluminum alloys during necking [49]. However, the strains in this study are small and less than the uniform strain. Additionally, our objective is to use the Y-U model, which is widely used in the automotive sector, and that has been shown to capture the Bauschinger effect accurately.

The present study focuses on quantitatively evaluating the performance of methods to calculate the parameters of the Yoshida-Uemori model and their sensitivities. Two advanced high-strength steels and two aluminum alloys were evaluated. The present contribution is part of the National Institute of Standards and Technology (NIST) effort [50–53] to generate test methods, data, and models for uniaxial, biaxial, and tension-compression testing of lightweighting alloys.

The paper proceeds as follows. A brief description of the experimental procedure is presented first. Then, two methods, Manual and Optimization, are presented for obtaining the Y-U parameters. The Manual Method is a reasonable approach for obtaining the Y-U parameters. However, as it will become evident later, the Optimization Method is a superior approach for obtaining the Y-U parameters. The predicted stress-strain curves from these methods are then both compared to results from a literature determination of the Y-U parameters that employed the same data set. The comparisons are both qualitative, using computed stress-strain curves, and quantitative, using the residual difference between the measured and computed curves. Finally, the sensitivities of the match between measured and computed stress-strain data to variations in the Y-U parameters are summarized.

2. Experimental procedure

2.1 Materials and Test Specimens

As part of the Numisheet 2020 benchmark exercises [54], and at the direction of the Benchmark Committee, NIST conducted monotonic uniaxial tension and tension-compression tests on Benchmark 1 (BM1) DP 980, Benchmark 2 (BM2) DP 1180, BM1 AA6XXX-T4, and BM2 AA6XXX-T81 alloy specimens. Reference [55] contains a complete description of the experimental configurations and tension and tension-compression data. The rest of Section 2 simply summarizes that report. All test specimens were fabricated by abrasive waterjet cutting. Figure 1 shows dimensions of the test specimens. The analysis of this study employed only test specimens that were oriented at zero degrees to the rolling direction of the sheets.

2.2 Testing

Each test was replicated three times. The actuator velocity was maintained at a rate to produce an engineering strain rate 2.5×10^{-4} (mm/mm)/s. Strains were measured using a virtual extensometer with nominal gauge length G=50 mm for the tension tests and G=23.8 mm for the tension-compression tests.

2.2.1 Uniaxial tension tests

The uniaxial tension tests were performed at constant engineering strain rate through failure. From the plots of true stress vs. true strain curves, the 0.2 % offset yield strength and Young's modulus were determined for each test, and the average values for each material were used in Manual Method of parameter fitting in Section 3.1.

2.2.2 Uniaxial tension-compression tests

Figure 2 shows the tension-compression test configuration. Anti-buckling guides (ABGs) lubricated by polytetrafluoroethylene (PTFE) sheet and petrolatum prevented out-of-plane buckling while minimizing friction effects. The left and right ABG pneumatic actuators applied a 3000 N side force to the wide faces of the test specimen through the ABGs for the entire test, which produced a compressive stress on the face of the specimen of approximately 2.5 MPa. The axial force was defined as the average readings of the upper and lower load cells. During the test, the difference between the forces indicated by the upper and lower load cells was typically not more than 1.6 %, about 200 N. In the most extreme case, it was 3.5 % of the maximum force.

The tension-compression test protocol, selected by the Numisheet Benchmark Committee, comprised three segments in displacement control. Segment 1 was a tensile stretch to a fixed displacement that produced a nominal engineering strain of 0.05 mm/mm for DP 980, AA6XXX-T4, and AA6XXX-T81. However, due to the limited ductility, the final nominal strain in segment 1 for the DP 1180 tests was 0.02 mm/mm. Then after a 10 s hold, segment 2 was compression to a fixed displacement determined to produce a final specimen engineering strain approximately zero. After another 10 s hold, segment 3 was a tension stretch until specimen failure. Ref. [55] provides additional details about the tests as well as the data. Measured true stress-true strain diagrams for all four materials from Ref. [55] are shown in Figure 3. Because segment 3, tension to failure, was not used in this analysis, it is not plotted. The stress-strain behavior of materials that exhibit tension-compression asymmetry will be different if segment 1 is compression, instead of tension; see for example Ref. [56]. These data are not available in Ref. [55], however.

2.2.3 Digital Image Correlation strain measurements.

A stereo Digital Image Correlation (DIC) system captured strain data for all tests. The speckle pattern was applied on the wide face of the tension specimens and on the narrow face of the tension-compression specimens. See Figure 4 for a graphical description of the tension-compression test configuration. The DIC analysis parameters were optimized with “Virtual Strain Gauge” studies, as recommended by the Good Practices Guide for DIC [57]. Stress-strain curves for both tension and tension-compression tests were created using a DIC-defined virtual extensometer, with gauge length, *G*, also shown in Figure 1.

2.2.4 Computational software

The Manual Method for determining the values of the Y-U parameters employed a script written in the commercial software package MATLAB. The Optimization Method analyses used the commercial finite-element analysis (FEA) software package, LS-DYNA, coupled to its optimization software, LS-OPT, hereafter referred to as the “commercial FEA package coupled to its optimization software.” Specifically, the package implemented the kinematic hardening, transversely anisotropic constitutive material model (MAT_125) [45]. The stress-strain curves were computed using the commercial FEA package LS-DYNA as well.

3 Y-U model parameters determination: methods and results

The focus in this paper is on the Y-U model, which involves determining ten parameters: Y, B, C, R_{sat}, b, h, k, E_0, E_{sat}, and ξ summarized in Table 1. Two methods were used. The Manual Method used three different approaches to estimate the ten parameters. Two parameters, Y and E_0, were determined from the tension stress-strain curves. Three parameters, *h*, E_{sat}, and ξ, were taken from literature values. The remaining five parameters, *B*, *C*, R_{sat}, *b*, and *k*, were extracted by fitting the forward (tension) and reverse (compression) segments of the tension-compression curve separately. In the Optimization Method, all nine parameters were fit simultaneously, and E_0 was determined from the tension stress-strain curves.

For both the Manual and Optimization Methods, the appropriateness of Y-U model parameters for predicting the stress-strain response was verified by creating predicted numerical stress-strain curves and comparing them to the experimentally determined curves. Ref. [58] used 100 square shell elements in commercial FEA package to model the uniform deformation region in a tension-compression test. However, a single element is often desirable in the FEA testing phase because it typically reduces convergence issues for a highly nonlinear problem. In addition, it is a preferred approach to test complex hyperelastic, creep, or plasticity material models, and it reduces convergence problems that might occur especially with badly warped elements possible during the compression cycle. Therefore, a single-element, finite-element model that employed the Y-U model was used to create the predicted curves for segments 1 (tension, forward) and 2 (compression, reverse).

3.1 Manual Method

3.1.1 Determination of the Y-U model parameters by the Manual Method

3.1.1.1 Determination of Y and E_0

In Ref. [28] an elastic limit value was used for the value of the radius of the yield surface, *Y*. Experimental determination of the elastic limit requires a series of loadings and unloadings to determine when plasticity begins. That process is both time consuming and lacks repeatability. Another option is to define the radius of the yield surface as the stress at the proportional limit, the deviation from linear stress-strain behavior. However, some very small nonlinear behavior can happen well before initial yield, which also leads to low repeatability of the value of *Y*. Therefore, many in the literature choose to use the 0.2 % offset yield value for the radius of the yield surface, *Y*, which is more repeatable, but overpredicts the initial yield. For the Manual Method, the average 0.2 % offset yield value from the monotonic uniaxial tests (as described in Section 2.2.1) was used for the value of the radius of the yield surface, *Y*, for each material. The value of the Young's modulus at the initial state, E_0, was set to the average value, Table 3, for each material of the three determinations in the uniaxial tension tests.

3.1.1.2 Determination of h, $E_{sat,}$ and ξ

For the dual-phase steel alloys, DP 980 and DP 1180, the values of E_{sat} and ξ were taken from literature values [4]. For the aluminum alloys, AA6XXX-T4 and AA6XXX-T81, the Manual Method neglected elastic modulus degradation, because no suitable values exist in the literature.

The parameter *h*, the fraction of hardening that is kinematic versus isotropic, can be determined from the experimental data of stress-strain curve in the plastic strain range of work-hardening stagnation (during the reverse transformation) or from studying the cyclic hardening characteristics (multiple tension-compression loops). Numerical simulation [4,58] showed that a large value of *h* results in prediction of smaller saturated stress amplitudes under cyclic loading. It is typically determined from a modeled best-fit match to the experimental data. In this study for the Manual Method, the value *h* = 0.5 was chosen as suggested by researchers [4,58].

3.1.1.3 Determination of B, C, R_{sat}, b, and k

The five remaining model parameters, *B, C*, R_{sat}, *b*, and *k* were determined by fitting the forward, and then the reverse, segments of the tension-compression stress-strain curves, using a script that used an approach of the minimization of error with a least-squares technique.

The forward bounding surface, the line connecting point b to point c in Figure 15a in the appendix, was fitted with equation 1, which is the same as equation A8, but is rewritten with the notation of $\sigma_{\mathrm{bound}}^{(\mathrm{fow})}$ for the forward bounding surface to match the notation used in Ref [28]:

$$\sigma_{\mathrm{bound}}^{(\mathrm{fow})} \quad = B + R + \beta = B + (R_{\mathrm{sat}} + b)(1 - e^{-k\varepsilon^{p}}) \tag{1}$$

By fitting the forward bounding curve of true stress vs. true plastic strain, obtained from the forward deformation with equation 1, (the type of equation is analogous to Voce-type hardening), the parameters *B*, (R_{sat} +*b*), and *k* were obtained.

From equation A7, the permanent softening at the start of reverse deformation, $\sigma_{B0}^{(\mathrm{p})}$, when $\varepsilon^{\mathrm{p}} = \varepsilon_0^{\mathrm{p}}$, i.e., $\hat{\varepsilon}^{\mathrm{p}} = -\left(\varepsilon^{\mathrm{p}} - \varepsilon_0^{\mathrm{p}}\right) = 0$ in Figure 15a, which is the difference between points j and k in Figure 15a and Figure 15b is given as:

$$\sigma_{B0}^{(\mathrm{p})} = 2\beta_0 = 2b\left(1 - e^{-k\varepsilon_0^{\mathrm{p}}}\right) \tag{2}$$

The reverse bounding curve was determined by extrapolating the true stress vs. true plastic strain curve from its saturation point as line e-j in Figure 15a. The point k in Figure 15a is known from the forward bounding curve; it is the mirror image of the point c. Hence the difference between point j and point k in Figure 15a is $2\beta_0$ in equation 2. Therefore, this value and the value of *k* from the fit of equation 1 determined the value of parameter *b*. Finally, R_{sat} was determined, since $(R_{\mathrm{sat}} + b)$ was known from the fit of the equation 1.

The value of the kinematic-hardening-rate parameter, *C,* was determined from the transient Bauschinger deformation as shown in Figure 15a. Researchers have used optimization methods for obtaining values of this parameter, and Yoshida and Uemori[28] provided equations for obtaining it. For the uniaxial case, the original back stress model of equation A2 results in the following equation:

$$\dot{\alpha}_* = C(a\dot{\varepsilon}^{\mathrm{p}} - \alpha_*|\dot{\varepsilon}^{\mathrm{p}}|) \tag{3}$$

where $\dot{\varepsilon}^{\mathrm{p}}$ is the plastic strain rate for the uniaxial deformation. It follows from this equation that the transient stress offset, $\sigma_{\mathrm{B}}^{(\mathrm{t})}$ in Figure 15a, which is the difference between the reverse stress-plastic strain curve (line d-e in Figure 15a) and the extrapolated curve of the permanent softening region (line e-j in Figure 15a), can be written as:

$$\sigma_{\mathrm{B}}^{(\mathrm{t})} = a + \alpha_* \approx 2ae^{-C\,\hat{\varepsilon}^{\mathrm{p}}} \tag{4}$$

where $\hat{\varepsilon}^{\mathrm{p}}$ is the reverse plastic strain. By fitting the $\sigma_{\mathrm{B}}^{(\mathrm{t})}$ vs. $\hat{\varepsilon}^{\mathrm{p}}$ curve (obtained from the reverse test data) with equation 4, the fitted values of coefficient *a* (i.e., *a=B+R-Y*) and the parameter *C* were determined.

3.1.1.4 Summary of Manual Method parameter values

Table 3 shows the values of the ten parameters (for DP 980 and DP 1180) and eight parameters (for AA6XXX-T4 and AA6XXX-T81) obtained using the Manual Method for all four materials and twelve tests. Except for the R_{sat} values for DP 1180, the parameters are in reasonable agreement between the replicate tests for each material, while the values of each parameter differ between materials, as expected.

The values of R_{sat}, the saturated value of the hardening at infinitely large plastic strain, reached very low values for DP 1180; in two tests its value was negative, which is not realistic. The hardening value decreased from the initial values for the bounding surface as a function of the plastic strain. The negative values arose because the measured stress-strain curve did not reach a plateau. The bounding-surface isotropic-hardening-rate exponent, *k,* controls the rate of isotropic hardening. The values of *k* are large, which indicates much faster isotopic hardening than that would normally be expected [4,58]. For DP 1180, the combination of values of *B*, *b*, and *k* represents the scenario where the bounding surface is predicted to harden isotopically in a rapid manner to a low saturated hardening of the bounding surface.

3.1.2 Verification of the Y-U model parameters determined by the Manual Method

To verify the appropriateness of the values of the Y-U model parameters in predicting the stress-strain response, the parameters determined by the Manual Method were used in the commercial FEA package that modeled the tension and compression segments of the measured stress-strain curve described in Section 2.2.2 using a single element. The resulting predicted stress-strain curves were compared to the measured tension-compression stress-strain curves.

The commercial FEA package used to verify the model parameters has implemented the Y-U constitutive model as a material model, which was used. (See Section 2.2.4.) A finite-element simulation of a cyclic, uniaxial tension-compression test was conducted with the FEA software. As explained earlier, to avoid issues such as buckling in the reverse deformation segment, the simulation used a square, one-element model, with a fully integrated four-node shell element that allows thickness stretch. The left bottom node was constrained in both x- and y-directions, while the right bottom node was constrained in x-direction. See Figure 5a. A uniform cyclic velocity (with equal positive and negative magnitude) boundary condition was applied in the y-direction on the two top nodes of this square element to simulate the cyclic, uniaxial loading conditions. A trial-and-error approach was used to determine the magnitudes of the velocity needed to produce the maximum strain observed in each test. Predicted axial normal y-true stress and mid-surface y-true strains at the element integration point were output and compared with measured true-stress-true-strain data for all tests included in this study.

Figure 6 compares the measured true stress vs. true strain curves to the computed curves from the FEA model that used the corresponding values of the Y-U model parameters as listed in Table 1 for each test. Qualitatively, the match for the forward deformation for the aluminum alloy tests is better compared to the steel tests. The deviation near the transition from the elastic to the plastic region is evident and is more pronounced for the dual-phase steel tests. The match for the reverse deformation for the dual-phase steel tests is not as good. The match for the DP 1180 steels is worse mainly because the test reached a strain level of 0.02 mm/mm (or 2 %), at which point the stress-strain curves did not reach a plateau, which is an inherent requirement for the determining the Y-U model parameters. One other main assumption of the Y-U model is that the shape of the stress-strain curve for the forward deformation is very similar to that for the reverse deformation. Although other researchers have also assumed this similarity [36,59–62], it may not be entirely true. The Y-U model traditionally predicts a slower change in work-hardening rate after initial yielding than that observed experimentally. This is the main cause of discrepancy between the measured and predicted curves because the same *C* values were used here for both the forward and reverse deformation. To circumvent this problem, Y-U [28] proposed a C_1+C_2 model, where the original kinematic-hardening-rate parameter C takes two different values, C_1 and C_2, for forward and reverse deformations respectively. The present study focused on the original Y-U model, with a single value of C, as there is not a fundamental approach for obtaining the C_2 parameter [28].

3.2 Optimization Method

Figure 6 indicates that while the qualitative match between the measured and predicted stress-strain curves for the Al-alloys is good, there are differences in the dual-phase steel curves, especially for the reverse deformation segment. It was difficult to stretch the DP 1180 steel specimens beyond 0.02 mm/mm strain without exceeding the uniform strain. Even in aluminum alloy curves, the match at the transition point between the elastic and plastic regions for the reverse stress-strain curve is poor. The problem with the Manual Method in Section 3.1.1 is that each segment of the curve (i.e., forward and reverse) was fitted separately. Consequently, the method could not provide a global picture that would include interdependence among the Y-U parameters for predicting both the forward and reverse deformation. Another unknown is which parameters are most sensitive and have the largest influence on the predicted stress-strain curve. Therefore, it was decided to further improve the values of these parameters by using a global optimization method that can also assess the parameter sensitivity, as explained below.

3.2.1 Determination of the Y-U model parameters by the Optimization Method

The goal here was to obtain the optimum values of the ten Y-U model parameters for each test, using both the forward and reverse segments simultaneously. A global Optimization Method, using the commercial finite-element package coupled to its optimization software was used to determine nine of the parameters: Y, B, C, R_{sat}, b, k, h, E_{sat}, and ξ . The value of the Young's modulus at the initial state, E_0, was again taken from the average of the three values determined in the tension tests. As described in 3.1.1, there is some disagreement in the literature whether to use the 0.2 % offset yield strength or the elastic limit for the radius of the yield surface, Y, of the Y-U model. For this reason, the value of Y was also selected as a design parameter, thus allowing the optimized value to potentially be closer to the unknown elastic limit.

The Optimization Method used curve mapping in the optimization software [63], which is appropriate for hysteretic curves. A one-element (hexahedral solid element) FEA model was used for obtaining the computed stress-strain curve. The solid element model was chosen as it removes the requirement of having to choose an arbitrary shell thickness in the shell element model. The side length of the element was 1 mm. The nodes at the bottom face were constrained in the y-direction, while the nodes at the left face were constrained in the x-direction, as shown in Figure 5b. A cyclic ramped velocity boundary condition in the y-direction was applied on the nodes at the top face of the element. The true stress vs. true strain values for this FEA solid-element model (y normal stress vs. y normal strain) for the cyclic loading tests were compared with measured values from the tests for the forward and reverse loading history.

A polynomial metamodel with linear order and D-optimal point selection was defined for the commercial optimization software predictive algorithm [63]. A metamodel is a mathematical approximation of computed results so that an optimizer can use predicted results (i.e., approximate results) for different combinations of design variable values without requiring additional FEA runs, saving overall computation cost of finding an optimum design. It is a mathematical function of design variables, and this function is obtained using regression analysis based on computed results of a few sample FEA runs. For traditional optimization based on a single scalar value, the metamodel predicts the response value (y) for a given design variable vector (x). In curve matching, since the output is history data (not a single value), a metamodel is constructed at each regression point of the curve so that we can obtain the entire "predicted" history for a given design variable vector (x). The regression points are the points used to fit a metamodel. In the context of curve matching, the regression points are the points along the curve where the error between test and computed curve is calculated. The optimizer uses these predicted histories instead of computed curves to minimize the error between the measured curve and the predicted curve. Note that the use of a metamodel is only to reduce the computation cost. In the case of the direct simulation-based curve matching (as opposed to metamodel-based curve matching), many FEA runs are needed for an optimum solution, thereby increasing computational cost significantly. The regression points are taken from the measured curves in the optimization software algorithm. The y-values from the measured curve were compared to interpolated points from the computed curve. This happens in normalized space to avoid biases when axis scales differ in magnitude for both the measured and computed curves.

Minimization of the residual that is defined as the sum of the vector of errors between the measured and computed curves was defined as the objective function, while the nine Y-U parameters (Y, B, C, R_{sat}, b, k, h, E_{sat}, and ξ) were the design parameters for the optimization algorithm. The curve-mapping error metric calculates the area between the computed curve and measured curve. The curves are normalized and if there are m regression points, then there are $m-1$ segments in the curves. The curves are therefore split into ($m-1$) segments, depending on the number of regression points (m). Each segment of the shorter curve is mapped to the longer curve, and the mapping distance between the segments of both curves is calculated. The segment length multiplied by this distance between the curves gives the area of mismatch between one segment along the two curves. This process is repeated for $m-1$ segments; the sum over all the segments represents the total error/mismatch/discrepancy in the curves, and this total error is selected as the objective for minimization [63].

For each Y-U model parameter, the optimization parameter spaces were defined as continuous with appropriate and realistic range of values for the specific parameter, summarized in Table 2. The ranges were selected by studying the values in the literature [4,28,29,58]. The optimization strategy was sequential response surface method (SRSM), where the actual optimization is an iterative process. A hybrid optimization algorithm was chosen, where the metamodel optimization started with an adaptive simulated annealing (ASA) algorithm to find an approximate global optimum after which a second leapfrog optimization algorithm (LFOP) was used to improve the solution[63]. Eight global iterations were specified. The Optimization Method specified two criteria: 1) change in the optimum objective values (between iteration n and $n-1$) < 0.01 and 2) change in the optimum design vector < 0.01.

The flowchart of the Optimization Method is shown in Figure 7. “Setup” is where the initial values and the range of values of the nine parameters (Y, B, C, R_{sat}, b, k, h, E_{sat}, and ξ) were defined (Table 2). The initial values were set to the values determined in the Manual Method. The objective for Optimization was defined in this case as minimization of the residual, i.e., the sum of the vector of the difference between the measured and model stress strain curves. In “Sampling” the metamodel was defined (a polynomial with linear order and D-optimal point selection technique). In “Solver” the FEA software was specified as the computation software; the nine design parameters were defined, and the three history data were designated to be extracted (i.e., stress, strain, and stress vs. strain data from the model). In "Build Metamodel" a mathematical model was actually constructed (as specified under "Sampling") for conducting a sensitivity study. In "Sensitivity Study" a global sensitivity analysis (GSA) was performed to calculate the sensitivity of a response with respect to selected design variables so that insignificant variables are eliminated before "Optimization." In "Convergence Test" the tolerance specified for termination is checked and whether maximum number of iterations was reached. This study specified design change tolerance = 0.01, objective function tolerance = 0.01, and maximum number of iterations = 8

In "Domain Reduction," to accelerate convergence, an adaptive domain reduction strategy is used to reduce the size of the subregion. Parameters for the Sequential with Domain Reduction (SRSM) method used are defined here. Additionally, the user can reset the subdomain range to the initial range values for a particular iteration and freeze the subdomain range from a particular iteration. The GSA results were evaluated using a large number of samples (10 000 by default) to obtain reasonable accuracy in sensitivity results. These samples were selected using Monte Carlo technique, which is simply a random point selection method. In "Verification" the final verification was conducted between the model prediction and the measured data. During the verification process, stress-strain data obtained from a FEA model with optimum design parameters were compared with test data to determine the quality of the fit. Note that a verification run of the predicted optimal design parameters was only conducted after the last full iteration and a successful convergence test. The "Verification" step is optional but is generally recommended as a good practice.

Table 3 shows the values of the nine Y-U parameters that were obtained by the Optimization Method. In general, the optimized Y values for Al alloys were within 10 % of the initial values from the Manual Method, but the values for the dual-phase steel decreased from the initial values by between 5 % and 28 %. This has to do with the nature of the hardening curves for dual-phase steels and their more gradual elastic to plastic transition. The optimized values of the bounding-surface isotropic-hardening-rate exponent, k, decreased overall from their initial values. The optimized values of the parameter h for Al alloy tests were lower than the assumed h=0.5 used in the Manual Method and were similar to the initial values for the dual-phase steels. The values of the parameters R_{sat}, b, and k for DP 1180 tests were highly variable between tests. This variability probably arose because a plateau was not reached in the stress-strain curve at the maximum strain level of 0.02 mm/mm. In the case of DP 1180 steels, the target range for optimization of these parameters was widened from typical ranges of parameter values reported in the literature by looking at the initial values of R_{sat}, b, and k obtained from the manual approach. (See Table 2.) These resulted in wide variability in values of these three parameters obtained using the optimization method for the three DP 1180 tests.

3.2.2 Verification of the Y-U model parameters determined by the Optimization Method

Figure 8 compares the measured stress-strain curves to those obtained from the Optimization Method with the optimized values of Y-U parameters listed in Table 3. Qualitatively, the match between the measured and computed stress-strain curves is much better compared to those from the Manual Method, shown in Figure 6. The match for the Al-alloy tests is nearly perfect. Although the match for the DP 980 tests is better for the Optimization Method than the Manual Method especially for the reverse deformation, noticeable disagreement still exists for the DP 1180 tests.

3.3 Numisheet Benchmark Study 2020 Method

The Numisheet Benchmark Study [54], which also used the stress-strain data [55] analyzed here, also reported a set of values of Y-U parameters computed by an optimization method of the commercial MatPara [64] software. The Numisheet Benchmark Study [54] did not report specific details of the optimization method, however. Instead of the single value for the parameter *C*, the reported set of values used the C_1+C_2 approach, equation 43a and 43b of Ref. [28], where individual values of the parameter *C* were used for the forward and reverse deformation segments. In contrast to the present study, the Benchmark Study reported only a single set of Y-U parameters for each of the four materials, as opposed to a set for each replicate test. Unfortunately, the values of C_1 and C_2 cannot be directly compared to the results for the single parameter value *C* from the Manual or Optimization Methods described in the present study. Therefore, all three Methods (Manual, Optimization, and Numisheet Benchmark Study) will be assessed based on the difference between the measured and computed stress-strain curves using the determined parameters.

3.3.1 Determination of the Y-U model parameters by the Numisheet Benchmark Study 2020 Method

Table 3 shows the values of the Y-U parameters taken directly from the Numisheet Benchmark Study [54], abbreviated as “NBS2020_Opt,” for all four materials, which used the same test data as the present study.

3.3.2 Verification of the Y-U model parameters determined by the Numisheet Benchmark Study 2020 method

Figure 9 compares the measured stress-strain curves to those obtained from the Numisheet Benchmark Study 2020 Method with the values of Y-U parameters from the Numisheet Benchmark Study [54] listed in Table 3. Qualitatively, the match between the measured and computed stress-strain curves using the Numisheet Benchmark Study 2020 Method is much better compared to those from the Manual Method, shown in Figure 6, and are qualitatively similar to that of the Optimization Method, shown in Figure 8.

4 Analysis

4.1 Summary of residual errors in the three methods

4.1.1 Difference plots

The quality of the fits from the Manual, Optimization, and Numisheet Benchmark Study 2020 Methods shown in Figure 6, Figure 8, and Figure 9 can be better visualized by a difference plot as shown in Figure 10 for the first replicated test (R01) of all four alloys. In Figure 10, the difference, $\Delta\sigma$, between the measured true stress, σ, and the computed true stress, σ_c, for each model is plotted separately for the forward and reverse deformation segments.

$$\Delta\sigma = \sigma - \sigma_c \tag{5}$$

Standard interpolation functions were used to calculate the computed stress at each measured strain point, because the number of abscissa values differ among the datasets. For both the forward and reverse deformation, the differences are large at the elastic/plastic transition region. Otherwise, the agreement is good in the fully developed plastic flow region, especially for AA6XXX-T4. The fit in the forward deformation is always better than in the reverse deformation, as evaluated by the maximum absolute difference. The agreement is best using the parameters determined by the Optimization

Method, though the maximum deviations for the Numisheet Benchmark Study 2020 Method are not much larger.

4.1.2 Quantification of the differences between measured and computed stress-strain curves

The commercial optimization software was used to reduce the difference between the measured and computed stress-strain curves to a single value for the entire curve to easily compare the deviations among curves. This was accomplished by computing a measure of the total deviation of the computed stress-strain curve from the measured stress-strain curve. As part of the curve-mapping process, the optimization algorithm reported the residual, δ, which is also called ε_p. (See chapter 28 of Ref. [63]). This value is essentially the difference in areas between the measured and computed curves, as described in Section 3.2.1, after the *x* and *y* values of both are normalized so that they vary from 0 to 1.

Figure 11 plots the value of the residual, δ, from Table 3 for each replicate stress-strain curve for all four materials and quantifies the qualitative features of Figure 10. For each material, the Optimization Method reduced the value of the residual, δ, compared to the Manual Method by more than an order of magnitude for the aluminum alloys, and by a factor of 3 and 7 for the DP 1180 and DP 980 respectively. Because Ref. [54] only provided a single set of Y-U parameters for all three replicates, Figure 11 omits the results of the Numisheet Benchmark Study 2020 Method.

Because one purpose of this study was to evaluate methods for obtaining one set of the Y-U parameters for each material, the performance of two variants of the Manual Method, three variants of the Optimization Method, and the Numisheet Benchmark Study 2020 Method were evaluated comparing against all the replicate tests using the same data:

- Manual Method: Average of Parameters variant
- Manual Method: Individual variant
- Optimization Method: Average of Parameters variant
- Optimization Method: Individual variant
- Optimization Method: Simultaneous variant
- Numisheet Benchmark Study 2020 Method

4.1.2.1 Average of Parameters Variant

In the Average of Parameters variant, the individual Y-U parameters for each replicate test of a given material were averaged to produce a single new set of Y-U parameters, also summarized in Table 3, which was then used to produce a new computed stress-strain curve. That computed curve was used to calculate the value of the residual, δ, for each of the stress-strain curves from the three replicate tests. The sum of the three residuals was calculated as the total residual for the variant, δ_{V} (in absolute values):

$$\delta_{\mathrm{V}} = \delta_1 + \delta_2 + \delta_3 \tag{6}$$

where $\delta_{i=1,2,3}$ are the residuals from the first, second, and third replicate tests.

4.1.2.2 Individual Variant

In the Individual variant, the individual Y-U parameters for replicate 1 for the Manual and Optimization Methods were used to compute a single stress-strain curve. From that curve, the total residual for the variant, δ_{V}, for the three replicates was calculated in the same way as for the Average of Parameters variant, equation 6. The Individual variant probes the behavior of the repeatability of the actual tension-compression test, because replicates 2 and 3 were not used to calculate the Y-U parameters.

4.1.2.3 Simultaneous Variant

In the Simultaneous variant, which was only possible with the Optimization Method, the Y-U parameters were calculated by optimizing the parameters against all three replicate curves simultaneously, instead of against just an individual curve. In this case the total residual for the variant, δ_V, for all three replicates is also what is being minimized as the goal of the optimization.

4.1.2.4 Numisheet Benchmark Study 2020 Method

In the Numisheet Benchmark Study 2020 Method, the Y-U parameters from [54] were used to compute a single stress-strain curve for each material. That computed curve was used to calculate the value of the residual, δ, for each of the stress-strain curves from the three replicate tests. The individual residuals, δ, were summed, equation 6, to compute the total residual for the variant, δ_V.

4.1.3 Summary of the performance of the variants

For all four materials, the optimization methods (Optimization and Numisheet Benchmark Study 2020) produced fits with residuals that were 2.5 to 12 times smaller than those from the corresponding Manual Method. (See Table 3.) Simultaneous Optimization always reduced the error by a factor between 1 and 2 compared to the Average of Parameters variant. Apart from the DP 1180 results, which suffered from the limited tension strain range, all both optimization methods performed quite well. (See Figure 12.) For the Manual Method, the total residual for the Average of Parameters variant, δ_V, were less than or equal to the individual residuals for all the materials except the DP 1180. For the Optimization Method, the total residual, δ_V, for the Average of Parameters variant was always higher than the individual determinations for all the materials, however the total residual, δ_V, for the Simultaneous variant was almost always equal to, or lower than, the individual determinations for all the materials. The Optimization Method and its variants either matched or outperformed the Numisheet Benchmark Study 2020 Method total residual results for all but the Average of Parameters variant for the dual-phase steels. This study shows that simultaneous optimization against all three test variants produced the least total residual values.

4.2 Y-U Model parameter sensitivity

A major goal of this paper is to determine which parameters have the most influence on the match between the computed and measured stress-strain responses. A global sensitivity analysis (GSA) was chosen over the correlation matrix approach. The correlation matrix can give some preliminary idea about sensitivity, but it does not necessarily imply causation. The global sensitivity analysis (GSA) is more rigorous. GSA results presented here are based on 10 000 regression points (a user-chosen number) selected using the Monte Carlo approach (a random point-selection method) and evaluated using the metamodel. The global sensitivity analysis was used to calculate the sensitivity of a design response with respect to selected design parameters so that insignificant variables are eliminated before optimization—the lower the number of variables, the lower the overall cost of performing the optimization. The GSA results were evaluated using a large number of samples to obtain reasonable accuracy. While other algorithms usually evaluate the integrand at regular grid points, the Monte Carlo approach randomly chose points at which the integrand was evaluated. This method is particularly useful for higher-dimensional integrals. Therefore, GSA results can show higher order effects. The parameters were scored based on their fractional influence on the response. For example, for the first design parameter, the fractional influence is its main contribution (main variance/total variance). Similarly, for the second parameter, the fractional influence is based on its main contribution plus interaction with the first parameter, and for the third parameter, the fractional influence is its main contribution plus interaction with the first variable plus interaction with the second variable, etc.

Figure 13 shows the results of the global sensitivity analysis of the Y-U parameters determined for each replicate in the Optimization Method. Data points show the mean value for the three replicates, and the bars show the minimum and maximum values. By shading, the body of the plot identifies regions of large (dark shading), small (light shading), and effectively no influence (no shading). Table 3 uses the same color scheme. For both aluminum alloys the influence of parameters *k*, followed by *B* are large, and R_{sat} has small influence. Other parameters have no influence. For DP 980 steel tests, three parameters have large influence: *B*, *C*, *k*. The influence of *Y* is small. The large-influence parameters in the DP 1180 tests are similar to those for DP 980, but the influence of parameter *b* is also large. Unlike DP 980, *Y* has effectively no influence while R_{sat} is seen to have a small influence.

In addition to the shading in Table 3 that highlights the level of influence, black boxes denote parameters that are at or very near minimum or maximum allowable limits for optimization. (See Table 2.) For the aluminum alloys, the parameters that reached these optimization limits had no influence on the optimization; therefore, these are not of much concern. The case of the DP 980 is similar except that the kinematic-hardening-rate parameter, *C*, had large influence but also frequently reached the optimization limit. This suggests either a larger optimization range or a different data set was needed to evaluate this parameter. In DP 1180, three parameters that had either large (*C* and *b*) or small (R_{sat}) influence also frequently reached an optimization limit. In this case, a different data set that extended to larger strain in the forward segment would have aided in the determination of more appropriate values of all three parameters.

For aluminum alloys, the global sensitivity analysis shows that bounding-surface isotropic-hardening rate exponent, *k*, is the parameter with the largest influence, signifying that global work hardening, i.e., formation of stable dislocation structures, is the dominant factor. Additionally, the initial radius of the bounding surface, *B*, is also important, because it dictates the initial value of the bounding stress and consequently, the radius of the yield surface. The small influence of the saturated value of the hardening at infinitely large plastic strain, R_{sat}, could be due by the fact that the strains in the tests were not large enough to produce saturation.

For the dual-phase steels, the influence of the initial radius of the bounding surface, *B*, and the bounding-surface isotropic-hardening-rate exponent, *k*, are large, like the aluminum alloys. However, the large influence of the kinematic-hardening-rate parameter, *C*, (transient Bauschinger deformation characterized by early re-yielding and subsequent change of work-hardening rate) signifies that motion of less stable dislocations, such as piled-up dislocations, is important for dual-phase steels. For DP 1180 steel, the large influence of the bounding-surface kinematic-hardening-rate parameter, *b*, signifies that the permanent softening and work-hardening stagnation caused by dissolution of dislocation cell walls and formation of new dislocation structures during reverse deformation is important to the constitutive behavior of this steel. Similar behavior for dual-phase steels was also reported in [27].

5. Summary, conclusions, and broader implications

5.1 Summary

This paper evaluated the performance of two methods, Manual and Optimization, for obtaining values of the constitutive-model parameters for Yoshida-Uemori (Y-U) isotropic-kinematic hardening model. The Y-U parameters were determined for two 6000-series aluminum alloys (AA6XXX-T4 and AA6XXX-T4) and two dual-phase steels (DP 980 and DP 1180) based on stress-strain data obtained from uniaxial tension and uniaxial tension-compression tests. In the first approach, a Manual Method was used to obtain these parameters by sequentially fitting the forward and then the reverse segments of stress-strain data obtained from tension-compression tests. In the second approach, an Optimization Method that used the curve-mapping feature of optimization software was used to obtain optimum values of the Y-U parameters by systematically reducing the difference between the measured stress-strain data and those computed from a one-element FEA model that employed those parameters. In addition, a third approach, termed the Numisheet Benchmark Study 2020 Method, computed stress-strain curves from a one-element model that employed literature values [54] of the Y-U parameters that had been computed from the same data set.

The performance of the methods was evaluated qualitatively by graphically comparing measured and computed stress-strain curves (Figure 6, Figure 8, and Figure 9), and quantitatively by evaluating the residual, δ, between the measured and computed curves (Figure 11). Although the quality of agreement for the Manual Method was generally good for each of the aluminum alloy tests fit individually, the agreement was inferior for each of the dual-phase steel tests when fit individually, especially for the reverse deformation segment. The Optimization Method produced better results, evaluated as the lower residual, δ, between the measured and computed stress-strain curves for each test. Several variants of the Manual and Optimization Methods were also evaluated to assess how well one set of parameters (from one test or the average of three tests) can reproduce all three replicate tests (Figure 12). However, applying the Optimization Method to all three replicate tests simultaneously produced the lowest total residual.

Statistical analyses conducted in conjunction with optimization studies established the relative influence each of the Y-U parameters on the overall agreement between measured and computed curves. For the aluminum alloys the most influential parameters were bounding-surface isotropic-hardening-rate exponent, k, followed by the initial radius of the bounding surface, B, and the saturated value of the hardening at infinitely large plastic strain, R_{sat}. For DP 980 steel tests, the most influential parameters were B, the kinematic-hardening-rate parameter, C, and k. For DP 1180 tests the trends were similar, except that the influence of the bounding-surface kinematic-hardening-rate parameter b was larger and that of C was somewhat smaller.

5.2 Conclusions

The Manual Method was inferior to Optimization Method for obtaining the values for the Y-U parameters, although it was relatively easy to implement. Averaging of the parameters from repeat tests could result in lower total residual than using parameters based on one test, however this was not always the case. Simultaneous optimization of the Y-U parameters against replicate stress-strain curves always produced fits that were better than averaging the values of the parameters from the individual fits.

The small strains achieved in the DP 1180 tests were likely the cause of the relatively poorer fits for the DP 1180 tests. The allowable ranges of the parameters, used for optimization constraint, had to be drastically expanded for the model to match the test data, which led to highly variable values for the saturated value of the hardening at infinitely large plastic strain, R_{sat}, the bounding-surface kinematic-hardening-rate parameter, b, and bounding-surface isotropic-hardening-rate exponent, k. (See Table 3.) In addition, some of the values were highly unlikely, e.g., $R_{sat} = 1$.

5.3 Broader Implications

Optimization methods, using a finite element model, like the one implemented in this manuscript, rather than the manual methods, should be used to determine the Y-U parameters, since those parameters will be eventually used in a finite element model to simulate a forming process. The higher-quality fits justify the small added difficulty. This is especially true when determining a single set of parameters for repeat tests.

The quality of the measured stress-strain data can strongly influence the optimum Y-U parameters. If the stress-strain curve fails to reach a saturation or plateau, spurious values of Y-U parameters can be generated. For this reason, replicate tests should be performed to diagnose potential problems, where separate fittings of each test will result in inconsistent sets of parameter values when the data quality is insufficient. Based on these results, a single stress-strain curve should never be used to determine the Y-U parameters. Either replicate tests or a combination of tests with different strain histories should always be used. Furthermore, the optimization to calculate the Y-U parameters should be carried out against all the replicate curves simultaneously rather than using the values of the parameters from any one of the individual tests, because this method produced a superior fit to all the data.

Appendix. The Yoshida-Uemori model

The Y-U model incorporates a two-surface modeling approach, where the yield surface moves within the so-called bounding surface in a kinematic manner. (See Section 1 and Figure 14.) Furthermore, only kinematic hardening is assumed for the yield surface, while mixed isotropic-kinematic hardening is assumed for the bounding surface. During plastic loading, both the bounding surface and the yield surface may move and change size. However, the bounding surface always encloses the yield surface. In cyclic tension-compression tests, the stress-strain responses are bounded by two lines in the uniaxial case. (See solid lines in Figure 15b.) In the multiaxial cases, the projections of the points generate a so-called bounding surface [38–40]. The region inside the yield surface corresponds to an elastic response. Plastic loading requires that the current stress point is located on the current yield surface boundary. The increase in the stress required to cause new plastic deformation because of the existence of the previous plastic deformation is known as strain hardening or work hardening. This is caused by dislocations interacting with each other and with barriers that impede their motion. It is well known that number of dislocations increases significantly in a crystal with increase in plastic strain. Dislocation pile-up on slip planes produces a “back stress,” which opposes the applied stress. Isotropic hardening of the bounding surface is due to the formation of these stable dislocation structures. The formation of these stable dislocation structures results in global work hardening. The Y-U constitutive model considers both translation and expansion of the bounding surface. On reverse loading, the material yields at a lower stress because the back stress developed during the forward deformation aids in dislocation movement when the deformation direction is reversed. Further softening occurs on stress reversal because dislocations of opposing signs attract and annihilate each other. This explains the well-known fact that the flow curve during reverse deformation is of less magnitude than the original, continuous flow curve in the forward direction. The reduction of the yield stress when the deformation in one direction is followed by deformation in the reverse or opposite direction is defined as the Bauschinger effect, which is characterized by early re-yielding that has been observed in tests. This early re-yielding is the reason why the Y-U model considers only kinematic hardening of the yield surface. The kinematic hardening of the yield surface is characterized by a rapid change of work-hardening rate, possibly due to two competing events: (a) creation of new dislocation structures during reverse deformation and (b) annihilation of dislocation structures created during the forward deformation.

To determine the necessary parameters for the Y-U model, a basic understanding of the specific purpose of each parameter involved is needed. Figure 14 shows a schematic of yield and bounding surfaces according to the Y-U model [28], and Table 1 lists the different parameters used in this model. In Figure 14, *O* is the original center of the yield surface; α defines the center of the current yield surface; β defines the center of the bounding surface; α_* refers to the relative kinematic motion of the yield surface in reference to the bounding surface. *B* is the initial radius of the bounding surface; *R* is the isotropic hardening parameter; *B*+*R* represents the current radius of the bounding surface; D^p is the plastic portion of the rate of deformation, and *Y* is the radius of the yield surface. The equations of this section, and in Figure 14 and Figure 15, preserve the notation that Yoshida and Uemori used. Figure 15a illustrates schematically the stress-strain response in a uniaxial forward-reverse deformation. The isotropic-kinematic hardening of the bounding surface is depicted in Figure 15b. The kinematic hardening of the yield surface is described as follows. The back stresses, α and β, can be expressed by the following equations. Note that the subscript (obj) represents the objective rate; for example, the objective stress rates are time derivatives of stress that do not depend on the frame of reference. Also note that the quantities that result from a double contraction operation such as the left-hand side quantities in equations A3 and A4 are defined with appropriate symbols with an overbar. This was done to preserve the notations used by Yoshida and Uemori [28].

$$\alpha_* = \alpha - \beta \tag{A1}$$

$$\alpha_{*,\mathrm{obj}} = C\left[\frac{a}{Y}(\sigma - \alpha) - \alpha_* \sqrt{\frac{a}{\overline{\alpha_*}}}\right]\dot{\overline{\varepsilon^{\mathrm{p}}}} \tag{A2}$$

$$\dot{\overline{\varepsilon^{\mathrm{p}}}} = \sqrt{\frac{2}{3} D^{\mathrm{p}} : D^{\mathrm{p}}} \tag{A3}$$

$$\overline{\alpha_*} = \phi(\alpha_*) = \sqrt{\frac{3}{2}\alpha_* : \alpha_*} \tag{A4}$$

$$a = B + R - Y \tag{A5}$$

where C is a material parameter that controls the kinematic-hardening rate; $\dot{\overline{\varepsilon^{\mathrm{p}}}}$ is the effective plastic strain rate; ϕ is a function of the Cauchy stress, and a represents the size difference between the bounding surface and the yield surface.

Y-U [28] used the following equation for the isotropic hardening of the bounding surface:

$$\dot{R} = k_{\mathrm{i}}\,(R_{\mathrm{sat}} - R)\,\dot{\overline{\varepsilon^{\mathrm{p}}}} \tag{A6}$$

where R_{sat} is the saturated value of the hardening at infinitely large plastic strain, and $\dot{R}$ is the rate of the isotropic hardening stress, *R*; k_i is a material parameter that governs the isotropic hardening rate of the bounding surface. Here as in Y-U [28], the value of k_i is assumed to be equal to the bounding-surface isotropic-hardening-rate exponent, *k*. Y-U assumed the following equation for the kinematic hardening of the bounding surface (assuming $k = k_{\mathrm{i}}$):

$$\beta_{\mathrm{obj}} = k\left(\frac{2}{3}\, b\, D^{\mathrm{p}} - \,\beta\, \dot{\overline{\varepsilon^{\mathrm{p}}}}\right) \tag{A7}$$

where *b* is the bounding-surface kinematic-hardening-rate parameter. For the case of uniaxial tension, the bounding surface is defined as:

$$\sigma_{\mathrm{bound}} = B + R + \beta = B + (R_{\mathrm{sat}} + b)\left(1 - e^{-k\varepsilon^{\mathrm{p}}}\right) \tag{A8}$$

where ε^{p} is the plastic strain. During reverse deformation, early re-yielding is followed by smooth elastic-plastic transition accompanied by a rapid change in work-hardening rate. This is also termed as non-isotropic hardening, which results in work-hardening stagnation. In the Y-U model, this work-hardening stagnation is assumed to develop due to the dissolution of the dislocation cell walls during the reverse loading. This work-hardening stagnation was expressed by the non-isotropic hardening of the bounding surface. The Y-U model accounts for this work-hardening stagnation with a non-isotropic hardening surface, $g(\sigma)$, in the stress space [28]. Note that isotropic hardening of the bounding surface is due to global work hardening, which is due to the formation of stable dislocation structures. The Y-U model also assumes that the center of the bounding surface, β, resides either on or inside $g(\sigma)$, which is referred as the consistency condition. Isotropic hardening of the bounding surface only takes place when the center of the bounding surface, β, stays on the boundary of $g(\sigma)$ [28][18]. Experimental observations [65,66]indicate that work-hardening stagnation increases with the accumulated plastic strain, which is expressed by the expansion of $g(\sigma)$ with increasing plastic strain. From the consistency condition stated above, the evolution equation of the radius of the non-isotropic hardening surface, *r,* can be expressed as

$$\dot{r} = h\,\frac{3(\beta - q)\,:\,\beta_{\mathrm{obj}}}{2r}\ \text{when}\ \dot{R} > 0$$

(A9)

$$\dot{r} = 0,\ \ \text{when}\ \ \dot{R} = 0$$

Note that *r* is not shown in Figure 14. A schematic illustration of non-isotropic hardening surface is shown in Ref. [28]. In Fig. 3 of Ref. [28], *q* denotes the center of the non-isotropic hardening surface. The material parameter *h*, which is the fraction of hardening that is kinematic versus isotropic, determines the rate of expansion of $g(\sigma)$and can assume values between 0 and 1. A larger value of *h* allows for the rapid expansion of the non-isotropic hardening surface, leading to smaller cyclic hardening.

The degradation of the elastic modulus during plastic deformation is considered in the Y-U model. It is important to consider this aspect when addressing a springback problem. Y-U proposed the following equation to describe the degradation of the Young's modulus, *E*:

$$E = E_0 - \ (E_0 - \ E_{\mathrm{sat}})\left[1 - e^{(-\xi\overline{\varepsilon^{\mathrm{p}}})}\right] \tag{A10}$$

where E_0 and E_{sat} are Young's modulus at the initial state and at infinitely large pre-strain respectively, and ξ is a material parameter that determines the degradation rate of Young's modulus with plastic strain.

Certain commercial equipment, instruments, or materials are identified in this paper in order to specify the experimental procedure adequately. Such identification is not intended to imply recommendation or endorsement by the National Institute of Standards and Technology, nor is it intended to imply that the materials or equipment identified are necessarily the best available for the purpose.

Acknowledgement

The authors thank Imtiaz Gandikota of ANSYS LST for many helpful discussions and suggestions during the implementation of the Optimization Method.

Data Availability Statement

The raw/processed data required to reproduce these findings cannot be shared at this time due to technical or time limitations. However, the data will be made available in the near future for download.

References

[1] J. Bauschinger, Changes of the elastic limit and the modulus of elasticity on various metals, Zivilingenieur. 27 (1881) 289–348.

[2] W.D. Carden, L.M. Geng, D.K. Matlock, R.H. Wagoner, Measurement of springback, Int. J. Mech. Sci. 44 (2002) 79–101. https://doi.org/10.1016/S0020-7403(01)00082-0.

[3] W. Gan, R.H. Wagoner, Die design method for sheet springback, Int. J. Mech. Sci. 46 (2004) 1097–1113. https://doi.org/10.1016/j.ijmecsci.2004.06.006.

[4] T. Phongsai, W. Julsri, B. Chongthairungruang, S. Suranuntchai, S. Jirathearanat, V. Uthaisangsuk, Identification of material parameters for springback prediction using cyclic tension–compression test, (2016) 9.

[5] X. Yu, H. Ji, H. Zhang, D. Xu, Experimental and numerical investigation on the Bauschinger effect during cold forming of TC4 ELI alloy, Int. J. Mater. Form. 15 (2022) 16. https://doi.org/10.1007/s12289-022-01666-8.

[6] T.J. Barrett, S. Takagi, N. Islam, T. Kuwabara, T. Hassan, B.L. Kinsey, M. Knezevic, Y.P. Korkolis, Material modeling and simulation of continuous-bending-under-tension of AA6022-T4, J. Mater. Process. Technol. 287 (2021) 116658. https://doi.org/10.1016/j.jmatprotec.2020.116658.

[7] F. Yoshida, T. Uemori, K. Fujiwara, Elastic–plastic behavior of steel sheets under in-plane cyclic tension–compression at large strain, Int. J. Plast. 18 (2002) 633–659. https://doi.org/10.1016/S0749-6419(01)00049-3.

[8] J. Zhu, S.Y. Huang, W. Liu, X.F. Zou, Semi-Analytical or Inverse Identification of Yoshida-Uemori Hardening Model, Key Eng. Mater. 775 (2018) 531–535. https://doi.org/10.4028/www.scientific.net/KEM.775.531.

[9] Y. Li, J. He, B. Gu, S. Li, Identification of advanced constitutive model parameters through global optimization approach for DP780 steel sheet, Procedia Eng. 207 (2017) 125–130. https://doi.org/10.1016/j.proeng.2017.10.749.

[10] J. Lin, Y. Hou, J. Min, H. Tang, J.E. Carsley, T.B. Stoughton, Effect of constitutive model on springback prediction of MP980 and AA6022-T4, Int. J. Mater. Form. 13 (2020) 1–13. https://doi.org/10.1007/s12289-018-01468-x.

[11] A. Aryanpour, M. Rodzik, D. Green, C. Van Tyne, L. Rothleutner, Characterization of Advanced High Strength Steel Sheets in View of the Numerical Prediction of Sidewall Curl, SAE Int. J. Mater. Manuf. 6 (2013) 90–98.

[12] P.-A. Eggertsen, K. Mattiasson, On constitutive modeling for springback analysis, Int. J. Mech. Sci. 52 (2010) 804–818. https://doi.org/10.1016/j.ijmecsci.2010.01.008.

[13] Q. He, Y. Chen, K. Ke, M.C.H. Yam, W. Wang, Experiment and constitutive modeling on cyclic plasticity behavior of LYP100 under large strain range, Constr. Build. Mater. 202 (2019) 507–521. https://doi.org/10.1016/j.conbuildmat.2018.12.146.
[14] C. Lu, Y.L. Kang, G.M. Zhu, Effect of Nonlinear Kinematic Hardening Model on Draw-Bend Springback Behavior of Dual Phase Steel, Adv. Mater. Res. 538–541 (2012) 448–452. https://doi.org/10.4028/www.scientific.net/AMR.538-541.448.
[15] J. Min, N. Guo, Y. Hou, K. Jiang, X. Chen, J.E. Carsley, J. Lin, Effect of tension-compression testing strategy on kinematic model calibration and springback simulation of advanced high strength steels, Int. J. Mater. Form. 14 (2021) 435–448. https://doi.org/10.1007/s12289-020-01583-8.
[16] Naofal, Naeini, Mazdak, Effects of Hardening Model and Variation of Elastic Modulus on Springback Prediction in Roll Forming, Metals. 9 (2019) 1005. https://doi.org/10.3390/met9091005.
[17] M.F. Shi, X. Zhu, C. Xia, T. Stoughton, Determination of nonlinear isotropic/kinematic hardening constitutive parameters for AHSS using tension and compression tests, in: 2008: pp. 264–70.
[18] M.F. Shi, L. Zhang, X. Zhu, Issues associated with the use of Yoshida nonlinear isotropic/kinematic hardening material model in Advanced High Strength Steels, J. Phys. Conf. Ser. 734 (2016) 032118. https://doi.org/10.1088/1742-6596/734/3/032118.
[19] X. Xia, M. Gong, T. Wang, Y. Liu, H. Zhang, Z. Zhang, Parameter Identification of the Yoshida-Uemori Hardening Model for Remanufacturing, Metals. 11 (2021) 1859. https://doi.org/10.3390/met11111859.
[20] P. Xu, H. Yu, H. Shi, H. Yu, Y. Wang, Kinematic hardening performance of 5052 aluminium alloy subjected to cyclic compression-tension, J. Phys. Conf. Ser. 1063 (2018) 012119. https://doi.org/10.1088/1742-6596/1063/1/012119.
[21] Q. Yin, A.E. Tekkaya, H. Traphöner, Determining cyclic flow curves using the in-plane torsion test, CIRP Ann. 64 (2015) 261–264. https://doi.org/10.1016/j.cirp.2015.04.087.
[22] H. Zhu, M. Huang, S. Sadagopan, H. Yao, Stress-Strain Characterization for Reversed Loading Path and Constitutive Modeling for AHSS Springback Predictions, J. Phys. Conf. Ser. 896 (2017) 012023. https://doi.org/10.1088/1742-6596/896/1/012023.
[23] S.-Y. Lee, S.-Y. Yoon, J.-H. Kim, F. Barlat, Calibration of Distortional Plasticity Framework and Application to U-draw Bending Simulations, ISIJ Int. 60 (2020) 2927–2941. https://doi.org/10.2355/isijinternational.ISIJINT-2020-391.
[24] Y. Yang, G. Vincze, C. Baudouin, H. Chalal, T. Balan, Strain-path dependent hardening models with rigorously identical predictions under monotonic loading, Mech. Res. Commun. 114 (2021) 103615. https://doi.org/10.1016/j.mechrescom.2020.103615.
[25] J.H. Choi, S.L. Zang, M.G. Lee, J.H. Kim, F. Barlat, Determining the coefficients of a homogeneous anisotropic hardening model for ultrathin steel sheets, Int. J. Mech. Sci. 157–158 (2019) 428–438. https://doi.org/10.1016/j.ijmecsci.2019.04.050.
[26] P.A. Prates, M.C. Oliveira, J.V. Fernandes, Identification of material parameters for thin sheets from single biaxial tensile test using a sequential inverse identification strategy, Int. J. Mater. Form. 9 (2016) 547–571. https://doi.org/10.1007/s12289-015-1241-z.
[27] D. Briesenick, M. Liewald, R. Radonjic, C. Karadogan, Enhanced accuracy in springback prediction for multistage sheet metal forming processes, in: J.P. Wulfsberg, W. Hintze, B.-A. Behrens (Eds.), Prod. Lead. Edge Technol., Springer, Berlin, Heidelberg, 2019: pp. 111–120. https://doi.org/10.1007/978-3-662-60417-5_11.
[28] F. Yoshida, T. Uemori, A model of large-strain cyclic plasticity describing the Bauschinger effect and workhardening stagnation, Int. J. Plast. 18 (2002) 661–686. https://doi.org/10.1016/S0749-6419(01)00050-X.

[29] F. Yoshida, T. Uemori, A model of large-strain cyclic plasticity and its application to springback simulation, Int. J. Mech. Sci. 45 (2003) 1687–1702. https://doi.org/10.1016/j.ijmecsci.2003.10.013.
[30] P.G. Hodge Jr., Discussion: “New Method of Analyzing Stresses and Strains in Work-Hardening Plastic Solids” (Prager, William, 1956, ASME J. Appl. Mech., 23, pp. 493–496), J. Appl. Mech. 24 (1956) 482–483. https://doi.org/10.1115/1.4011571.
[31] P. Armstrong, C. Frederick, A Mathematical Representation of the Multi Axial Bauschinger Effect., Central Electricity Generating Board, 1966.
[32] L. Geng, R.H. Wagoner, Springback Analysis with a Modified Hardening Model, in: SAE International, 2000. https://doi.org/10.4271/2000-01-0768.
[33] I. Ishlinski, General theory of plasticity with linear strain hardening, Ukr Math Zh. 6 (1954) 314–324.
[34] W. Prager, A New Method of Analyzing Stresses and Strains in Work-Hardening Plastic Solids, J. Appl. Mech. 23 (1956) 493–496. https://doi.org/10.1115/1.4011389.
[35] A.E. Green, P.M. Naghdi, A general theory of an elastic-plastic continuum, Arch. Ration. Mech. Anal. 18 (1965) 251–281. https://doi.org/10.1007/BF00251666.
[36] Z. Mróz, On the description of anisotropic workhardening, J. Mech. Phys. Solids. 15 (1967) 163–175. https://doi.org/10.1016/0022-5096(67)90030-0.
[37] W.D. Iwan, On a Class of Models for the Yielding Behavior of Continuous and Composite Systems, J. Appl. Mech. 34 (1967) 612–617. https://doi.org/10.1115/1.3607751.
[38] Y.F. Dafalias, E.P. Popov, A model of nonlinearly hardening materials for complex loading, Acta Mech. 21 (1975) 173–192. https://doi.org/10.1007/BF01181053.
[39] Y.F. Dafalias, E.P. Popov, Plastic Internal Variables Formalism of Cyclic Plasticity, J. Appl. Mech. 43 (1976) 645–651. https://doi.org/10.1115/1.3423948.
[40] Y.F. Dafalias, E.P. Popov, Cyclic loading for materials with a vanishing elastic region, Nucl. Eng. Des. 41 (1977) 293–302. https://doi.org/10.1016/0029-5493(77)90117-0.
[41] R.D. Krieg, A Practical Two Surface Plasticity Theory, J. Appl. Mech. 42 (1975) 641–646. https://doi.org/10.1115/1.3423656.
[42] Y.F. Dafalias, A bounding surface plasticity model, in: Proc. Seventh Can. Congr. Appl. Mech., Sherbrooke, Canada, 1979: pp. 89–90.
[43] S. Toros, Parameters Determination of Yoshida Uemori Model Through Optimization Process of Cyclic Tension-Compression Test and V-Bending Springback, Lat. Am. J. Solids Struct. 13 (2016) 1893–1911. https://doi.org/10.1590/1679-78252916.
[44] Z. Deng, Comparative Investigation on Aluminum Material Modeling with applications to Springback Prediction, IOP Conf. Ser. Mater. Sci. Eng. 967 (2020) 012012. https://doi.org/10.1088/1757-899X/967/1/012012.
[45] Livermore Software Technology Corp., LS-DYNA KEYWORD USER’S MANUAL VOLUME II Material Models, LIVERMORE SOFTWARE TECHNOLOGY Corporation, 2022. https://ftp.lstc.com/anonymous/outgoing/jday/manuals/DRAFT_Vol_II.pdf (accessed April 15, 2022).
[46] Springback of High Strength Steel with PAM-STAMP, (n.d.). https://www.esi.com.au/software/pamstamp-features/springback-hss/ (accessed June 2, 2022).
[47] Precise springback prediction of high tensile materials by using the Y-U model, (n.d.). https://www.jsol-cae.com/en/product/manufacturing/jstamp/cases/caseA06/index.html#breadcrumb (accessed June 2, 2022).
[48] B. Reyne, F. Barlat, A new concept for continuum distortional plasticity, Int. J. Plast. 155 (2022) 103303. https://doi.org/10.1016/j.ijplas.2022.103303.

[49] H. Aretz, A simple isotropic-distortional hardening model and its application in elastic–plastic analysis of localized necking in orthotropic sheet metals, Int. J. Plast. 24 (2008) 1457–1480. https://doi.org/10.1016/j.ijplas.2007.10.002.
[50] D. Banerjee, M. Iadicola, A. Creuziger, T. Foecke, Finite Element Modeling of Deformation Behavior of Steel Specimens under Various Loading Scenarios, Key Eng. Mater. 651–653 (2015) 969–974. https://doi.org/10.4028/www.scientific.net/KEM.651-653.969.
[51] D. Banerjee, M. Iadicola, A. Creuziger, T. Foecke, An Experimental and Numerical Study of Deformation Behavior of Steels in Biaxial Tensile Tests, in: TMS 2015 144th Annu. Meet. Exhib., Springer International Publishing, Cham, 2016: pp. 279–288. https://doi.org/10.1007/978-3-319-48127-2_35.
[52] D.K. Banerjee, C.A. Calhoun, M.A. Iadicola, W.E. Luecke, T.J. Foecke, Toward development of optimum specimen designs and modeling of in-plane uniaxial compression testing of aluminum alloy 2024 and AISI 1008 steel sheet material, J. Phys. Conf. Ser. 1063 (2018) 012068. https://doi.org/10.1088/1742-6596/1063/1/012068.
[53] A. Creuziger, M.A. Iadicola, T. Foecke, E. Rust, D. Banerjee, Insights into Cruciform Sample Design, JOM. 69 (2017) 902–906. https://doi.org/10.1007/s11837-017-2261-6.
[54] NUMISHEET2022: Benchmark Tests, (n.d.). https://www.tms.org/portal/MEETINGS___EVENTS/TMS_Meetings___Events/Upcoming_TMS_Meetings/NUMISHEET2021/benchmarkTests/portal/Meetings___Events/2021/NUMISHEET2021/benchmarkTests.aspx?hkey=8f0cff3e-b467-47d3-8f34-eb4d791ed9a5 (accessed April 15, 2022).
[55] M.A. Iadicola, Data for Numisheet 2020 uniaxial tensile and tension/compression tests, (2020). https://doi.org/10.18434/M32202.
[56] T. Maeda, N. Noma, T. Kuwabara, F. Barlat, Y.P. Korkolis, Measurement of the strength differential effect of DP980 steel sheet and experimental validation using pure bending test, J. Mater. Process. Technol. 256 (2018) 247–253. https://doi.org/10.1016/j.jmatprotec.2018.02.009.
[57] E.M.C. Jones, Iadicola, Mark A., eds., A Good Practices Guide for Digital Image Correlation, International Digital Image Correlation Society, 2018. https://doi.org/10.32720/idics/gpg.ed1 (accessed April 15, 2022).
[58] C.-Y. Chang, M.-H. Ho, P.-C. Shen, Yoshida–Uemori material models in cyclic tension–compression tests and shear tests, Proc. Inst. Mech. Eng. Part B J. Eng. Manuf. 228 (2014) 245–254. https://doi.org/10.1177/0954405413499011.
[59] N. Ohno, J.-D. Wang, Kinematic hardening rules with critical state of dynamic recovery, part I: formulation and basic features for ratchetting behavior, Int. J. Plast. 9 (1993) 375–390. https://doi.org/10.1016/0749-6419(93)90042-O.
[60] J.L. Chaboche, G. Rousselier, On the Plastic and Viscoplastic Constitutive Equations—Part I: Rules Developed With Internal Variable Concept, J. Press. Vessel Technol. 105 (1983) 153–158. https://doi.org/10.1115/1.3264257.
[61] J.L. Chaboche, G. Rousselier, On the Plastic and Viscoplastic Constitutive Equations—Part II: Application of Internal Variable Concepts to the 316 Stainless Steel, J. Press. Vessel Technol. 105 (1983) 159–164. https://doi.org/10.1115/1.3264258.
[62] Z. Hu, Work-hardening behavior of mild steel under cyclic deformation at finite strains, Acta Metall. Mater. 42 (1994) 3481–3491. https://doi.org/10.1016/0956-7151(94)90480-4.
[63] N. Stander, A. Basudhar, W. Roux, K. Liebold, T. Eggleston, T. Goel, K. Craig, LS-OPT 7.0 User Manual, 2020. https://www.lsoptsupport.com/documents/manuals/ls-opt/lsopt_70_manual.pdf (accessed April 15, 2022).
[64] Computation and Experimental Mechanics, MatPara. (n.d.). http://www.cem-inst.com/ (accessed April 18, 2022).

[65] N. Christodoulou, O.T. Woo, S.R. MacEwen, Effect of stress reversals on the work hardening behaviour of polycrystalline copper, Acta Metall. 34 (1986) 1553–1562. https://doi.org/10.1016/0001-6160(86)90100-8.
[66] Z. Hu, E.F. Rauch, C. Teodosiu, Work-hardening behavior of mild steel under stress reversal at large strains, Int. J. Plast. 8 (1992) 839–856. https://doi.org/10.1016/0749-6419(92)90006-X.

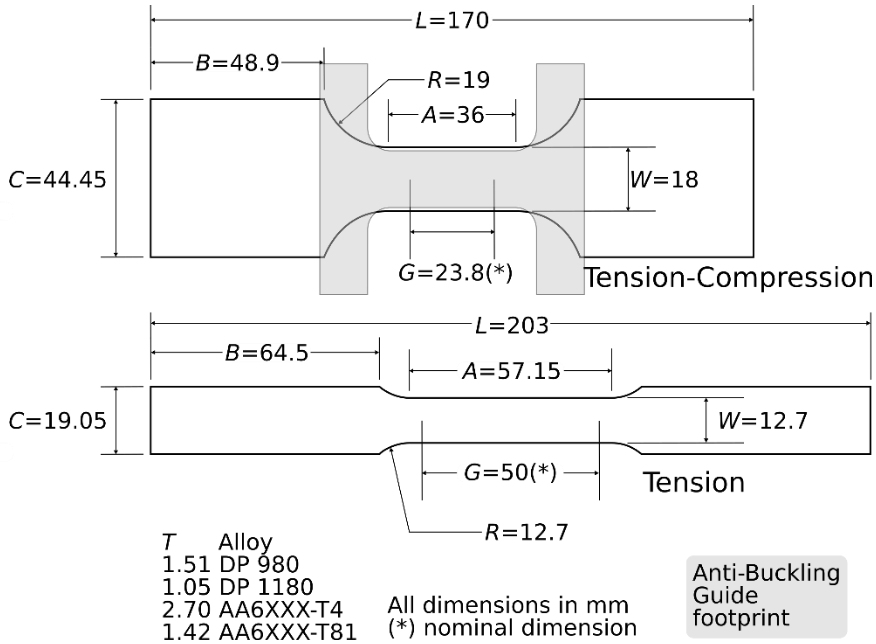

Figure 1 Test specimen nominal dimensions for tension and tension-compression tests.

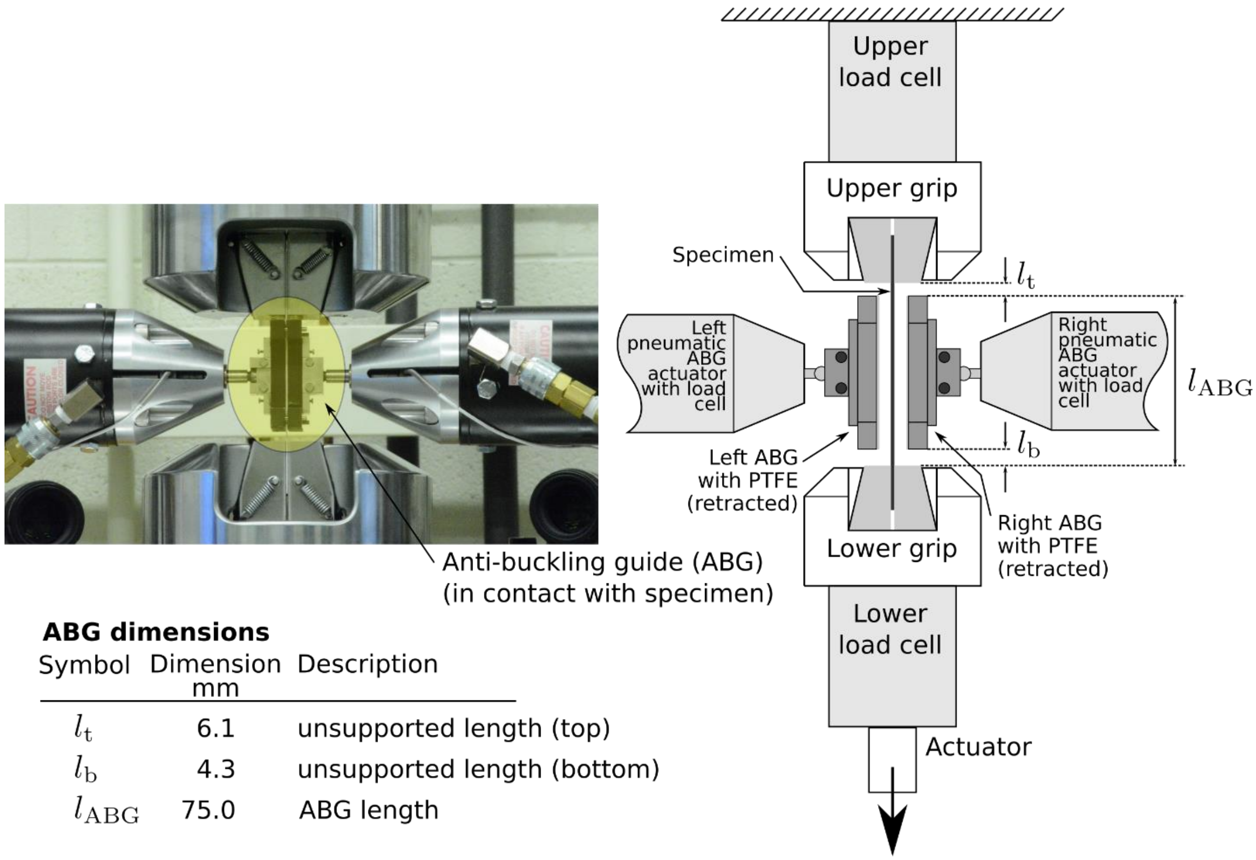

ABG dimensions

Symbol	Dimension mm	Description
l_t	6.1	unsupported length (top)
l_b	4.3	unsupported length (bottom)
l_{ABG}	75.0	ABG length

Figure 2 A close-up view of the tension-compression testing machine anti-buckling guides.

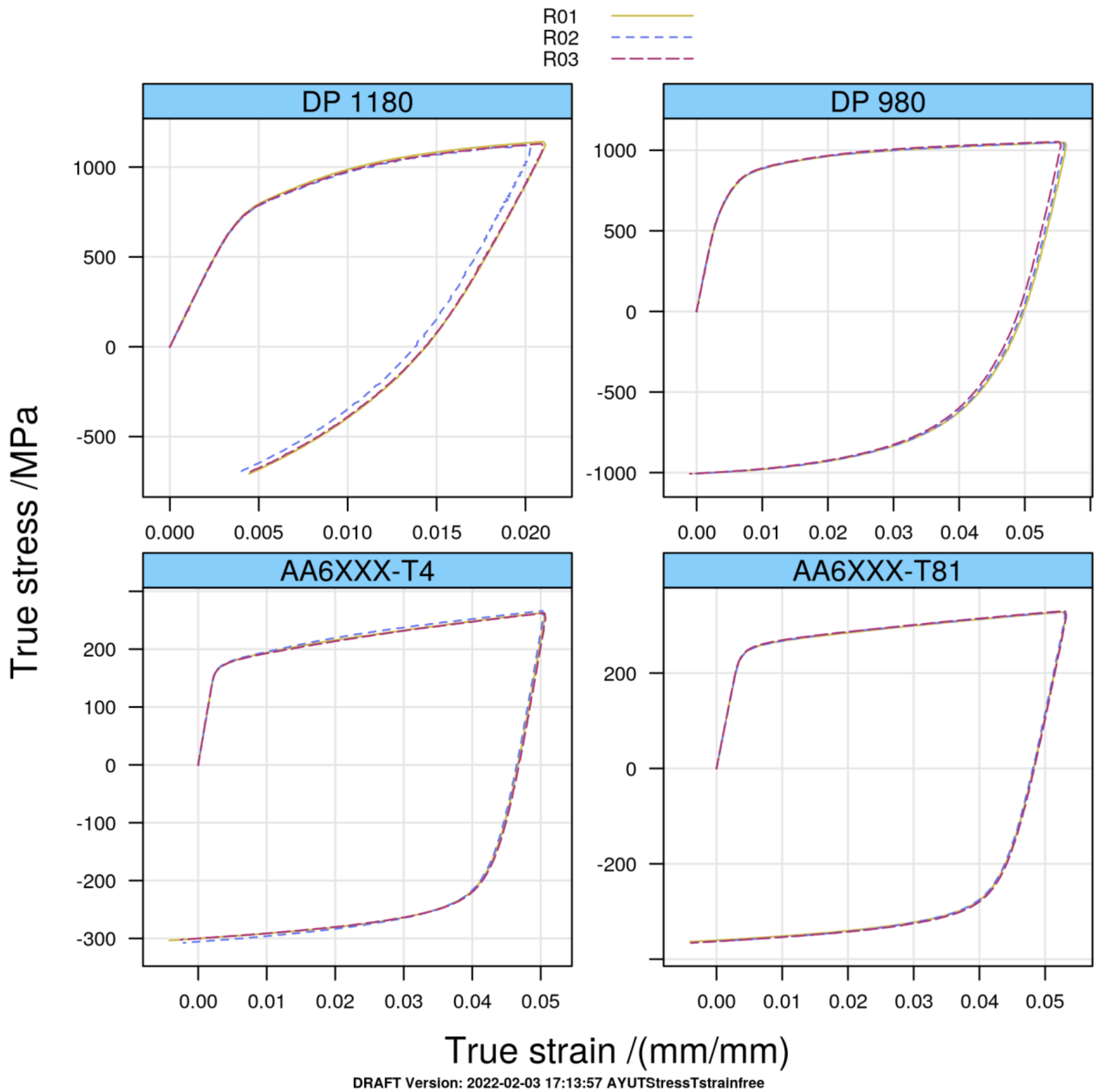

Figure 3 A plot of true stress vs. true strain from three replicate tension-compression tests on all four alloys.

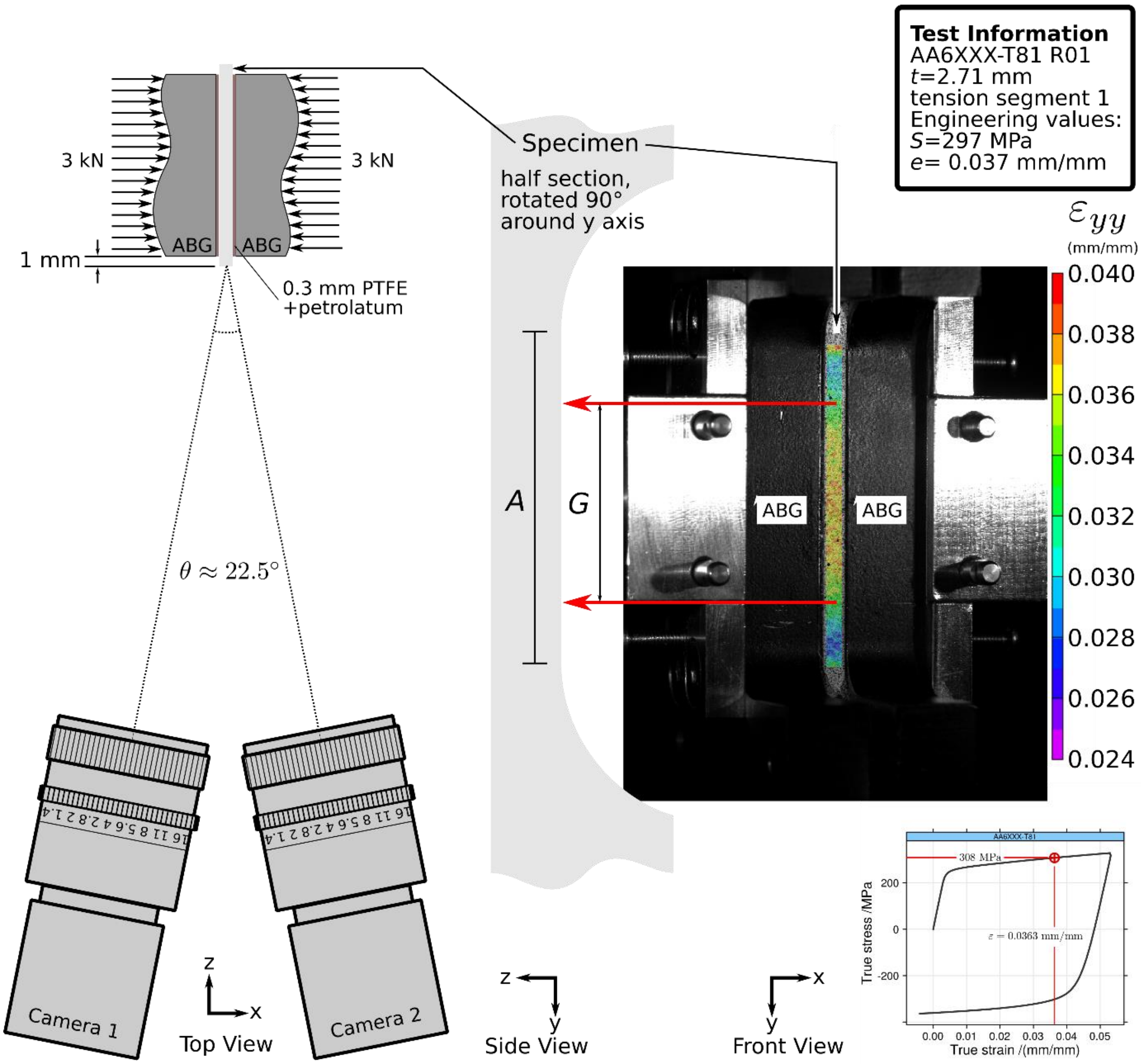

Figure 4 A schematic of the DIC strain measurement system used for tension-compression testing, along with typical image (from Camera 1 perspective) with DIC true strain contour map on an image of the specimen plus anti-buckling guides. The specimen outline in the side view image shows the relative positions of the gauge length on the same scale as the specimen in the front view. The plot in the lower right corner shows the point on the stress-strain curve that corresponds to the strain map.

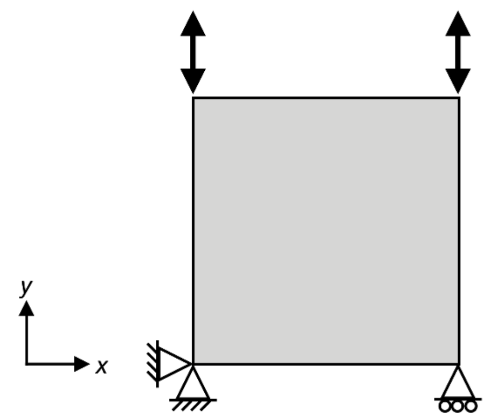

(a)

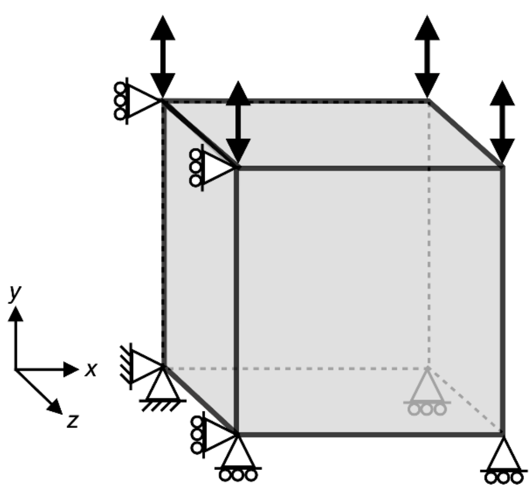

(b)

Figure 5 Single-element boundary conditions for (a) shell and (b) solid elements.

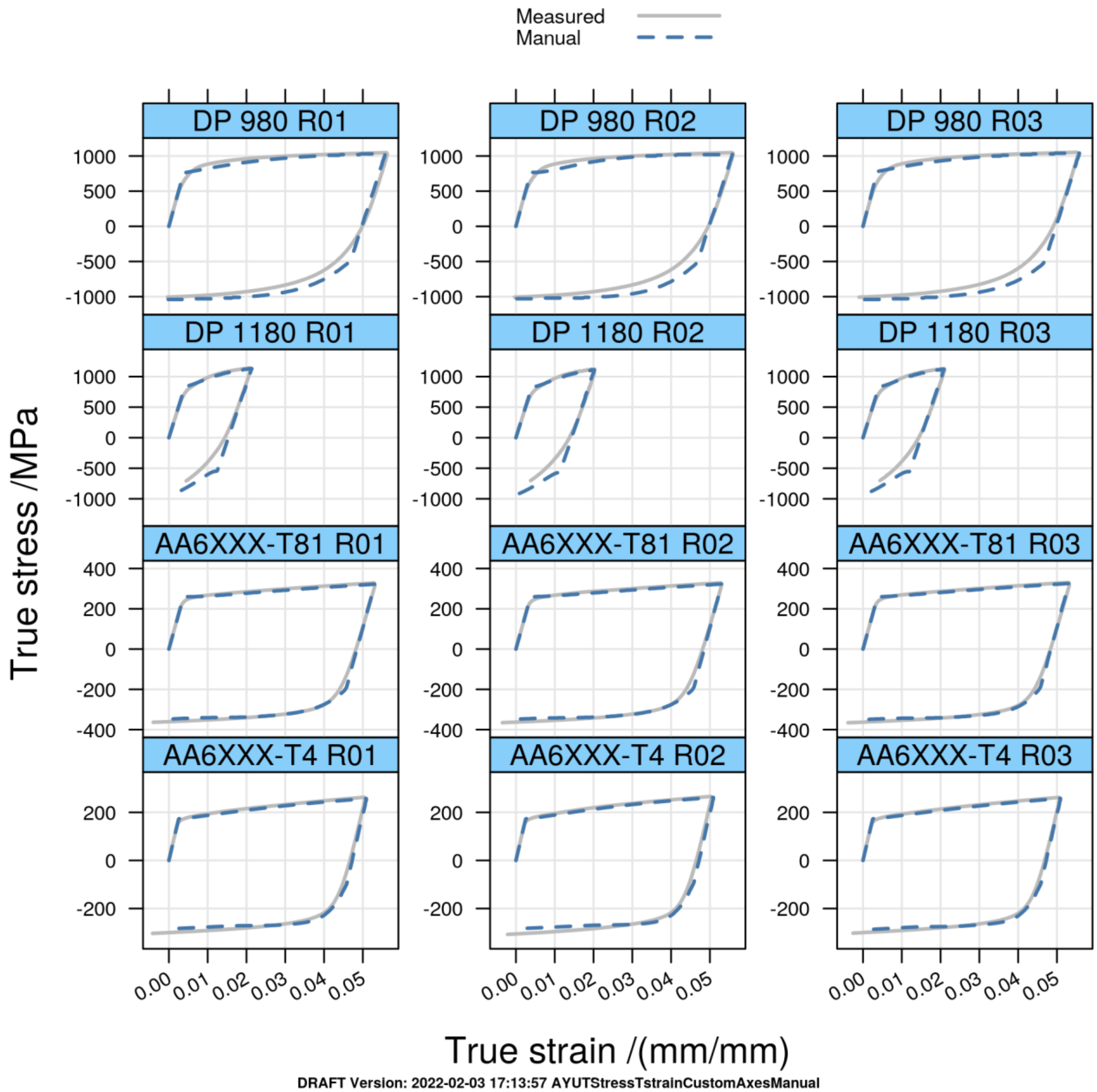

Figure 6 Comparison of measured true stress vs. true strain data and FEA-computed true-stress-true-strain data determined using the Y-U parameters from the Manual Method for top to bottom: DP 980, DP 1180, AA6XXX-T81, and AA6XXX-T4.

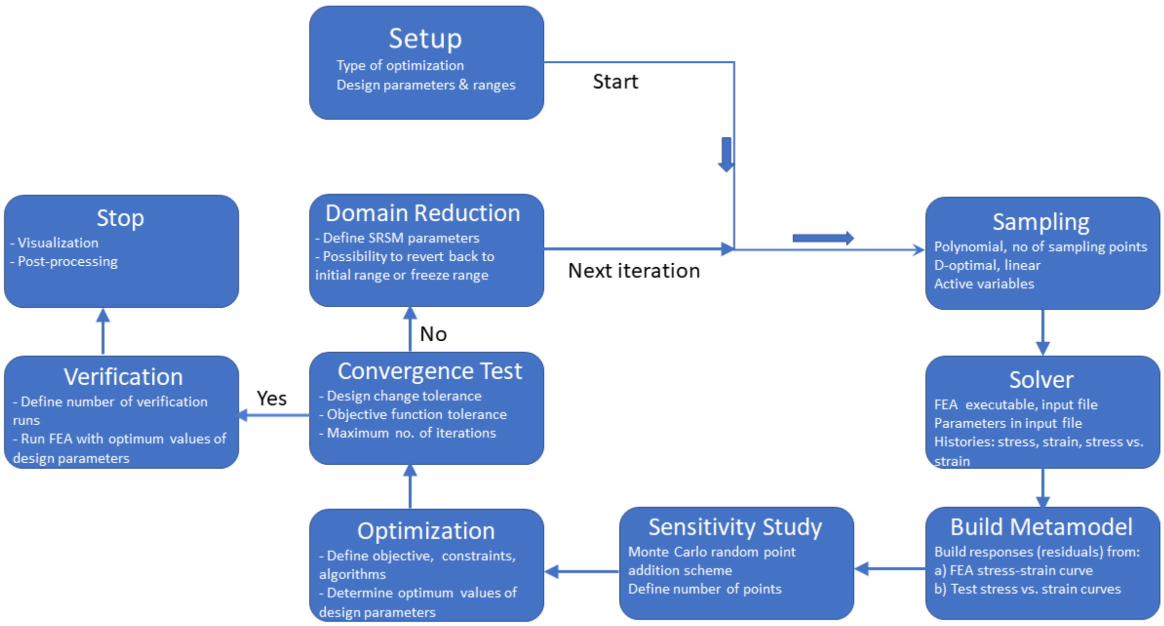

Figure 7 Flow chart for the Optimization Method.

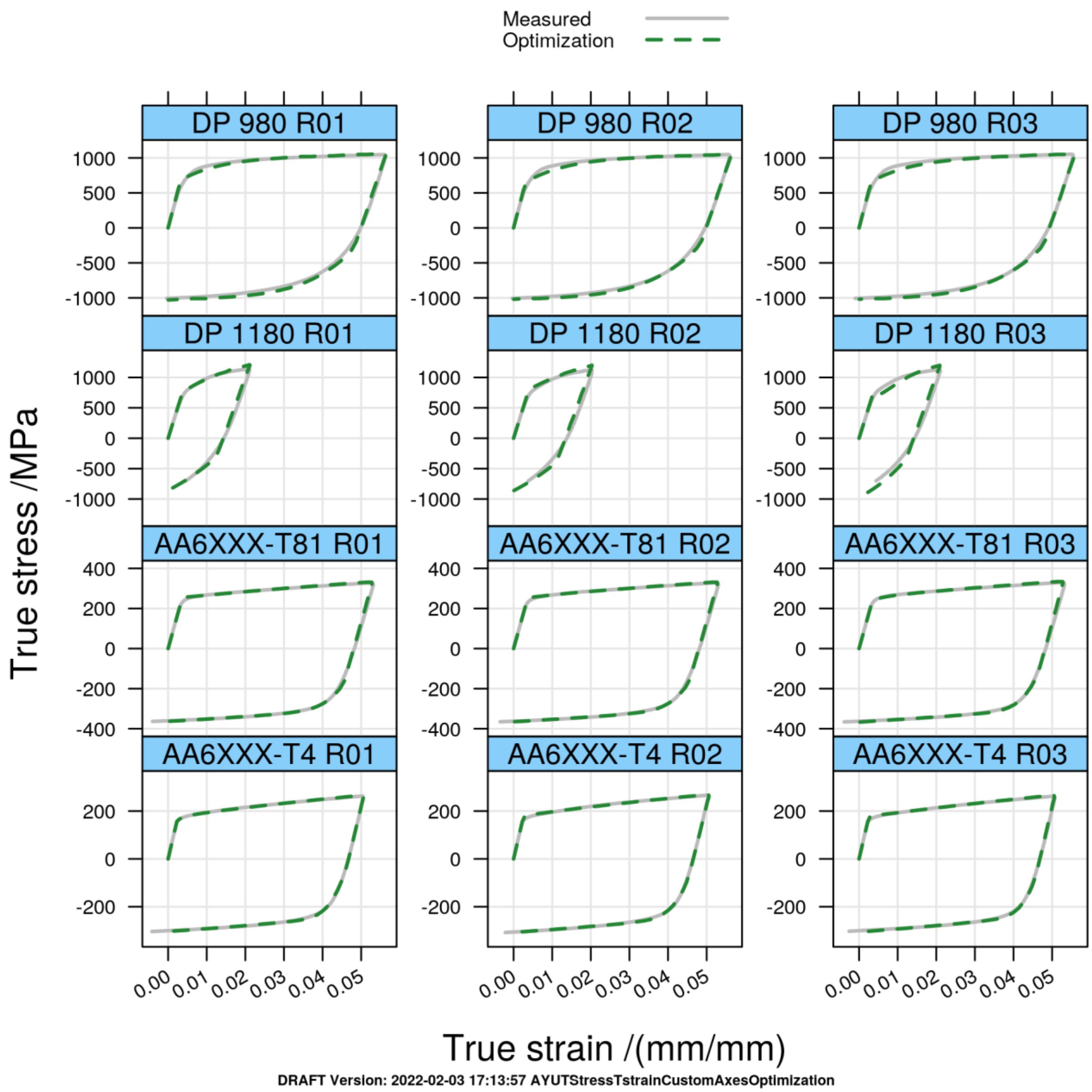

Figure 8 Comparison of measured true stress vs. true strain data and FEA-computed true-stress-true-strain data determined using the Y-U parameters from the Optimization Method for top to bottom: DP 980, DP 1180, AA6XXX-T81, and AA6XXX-T4.

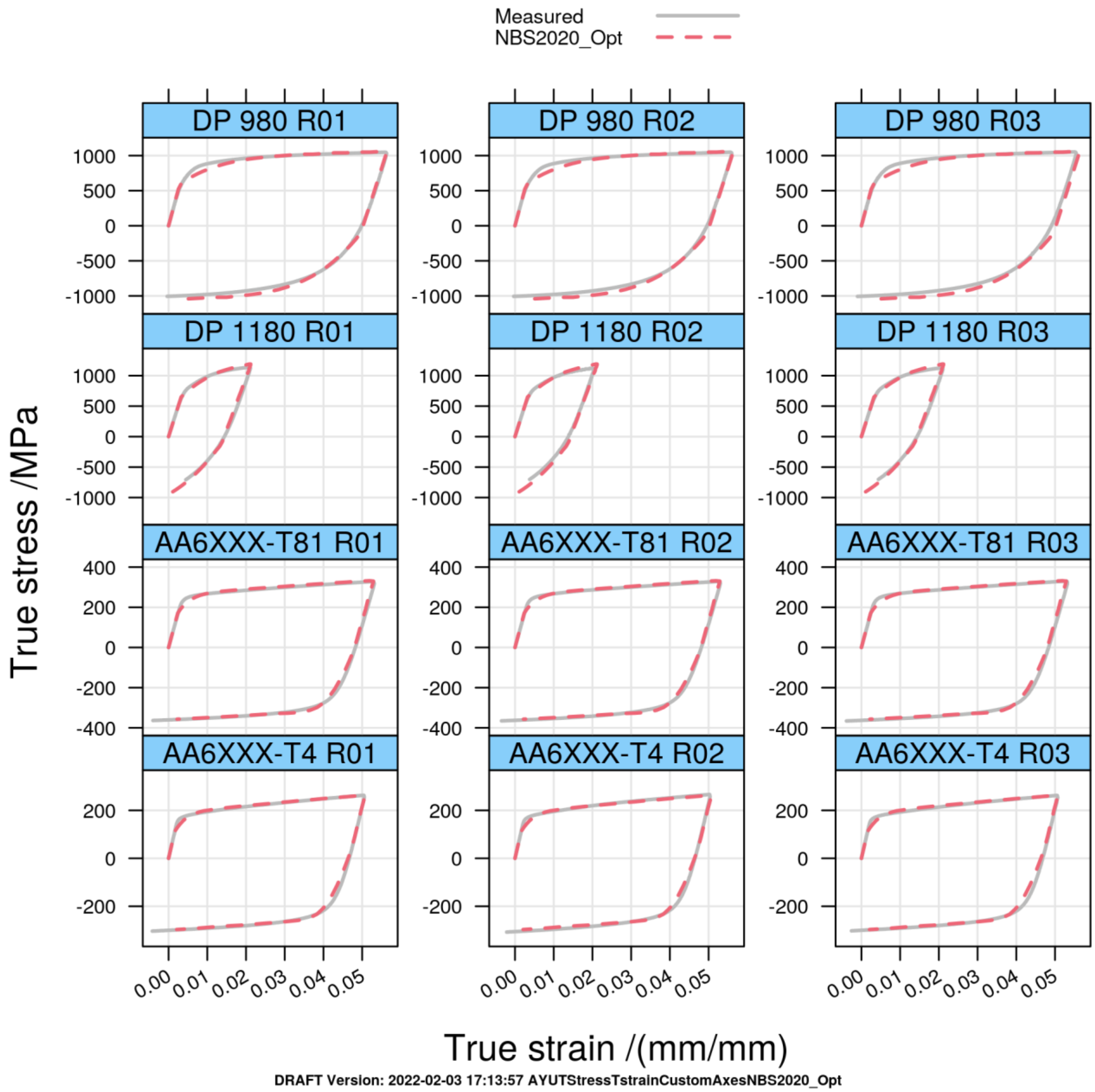

Figure 9 Comparison of measured true stress vs. true strain data and FEA-computed true-stress-true-strain data determined using the Y-U parameters from the Numisheet Benchmark Study 2020 Method, abbreviated NBS2020_Opt, for top to bottom: DP 980, DP 1180, AA6XXX-T81, and AA6XXX-T4.

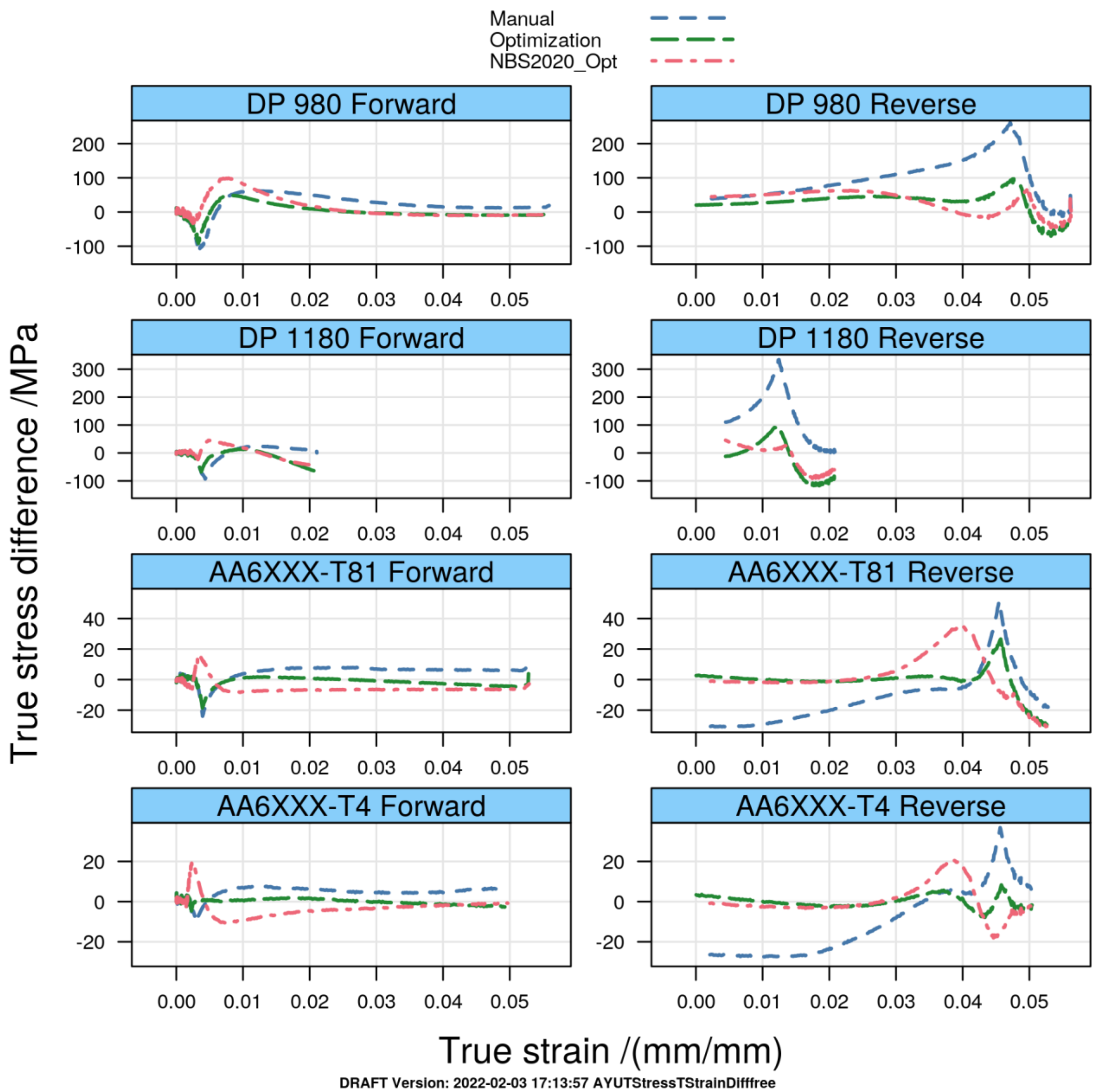

Figure 10 Comparison of difference between measured and computed stress-strain curves for all three methods.

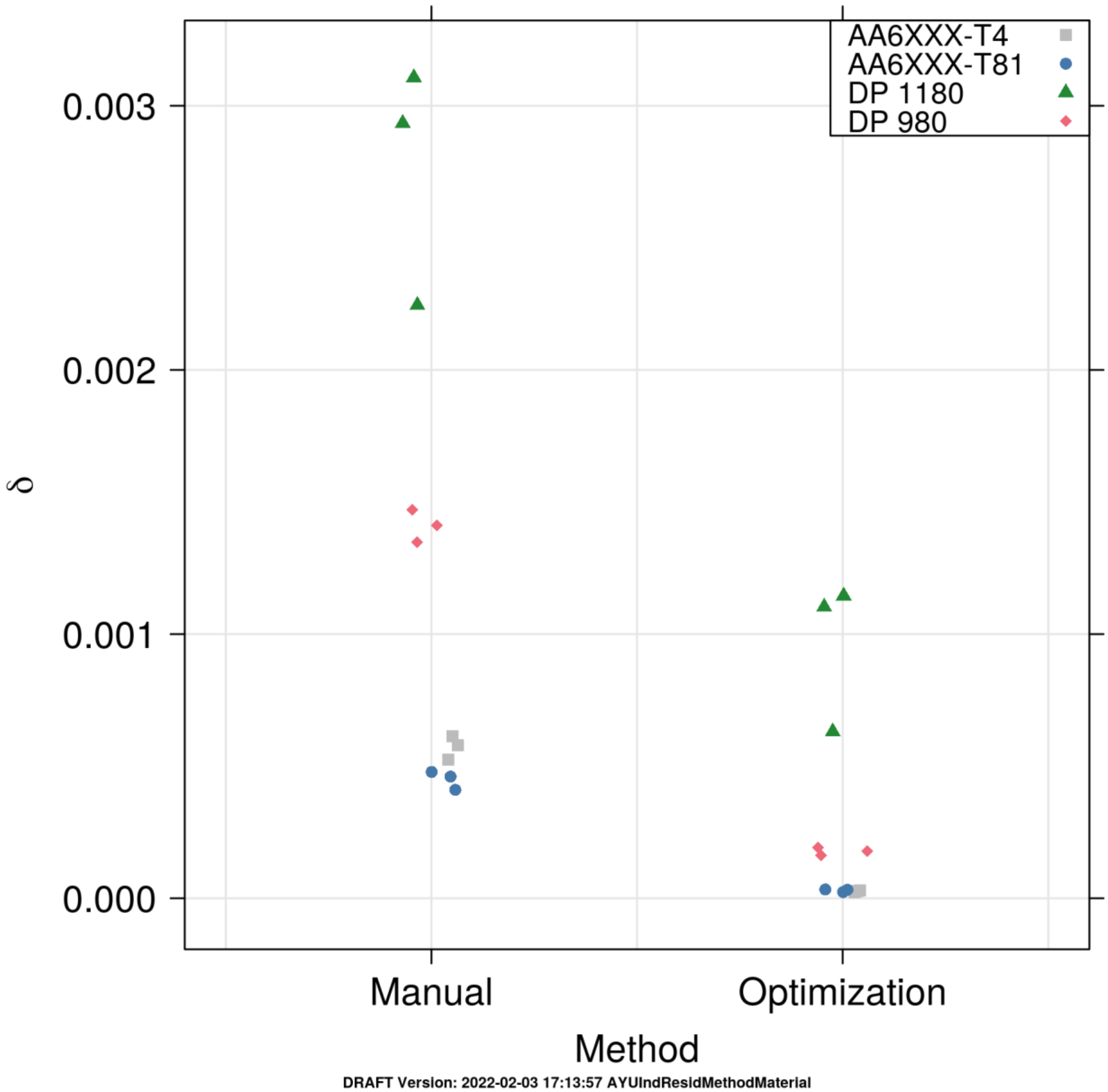

Figure 11 Residual (normalized), δ, for each stress-strain curve for each Method grouped by material. The x-axis values are shifted to minimize overplotting.

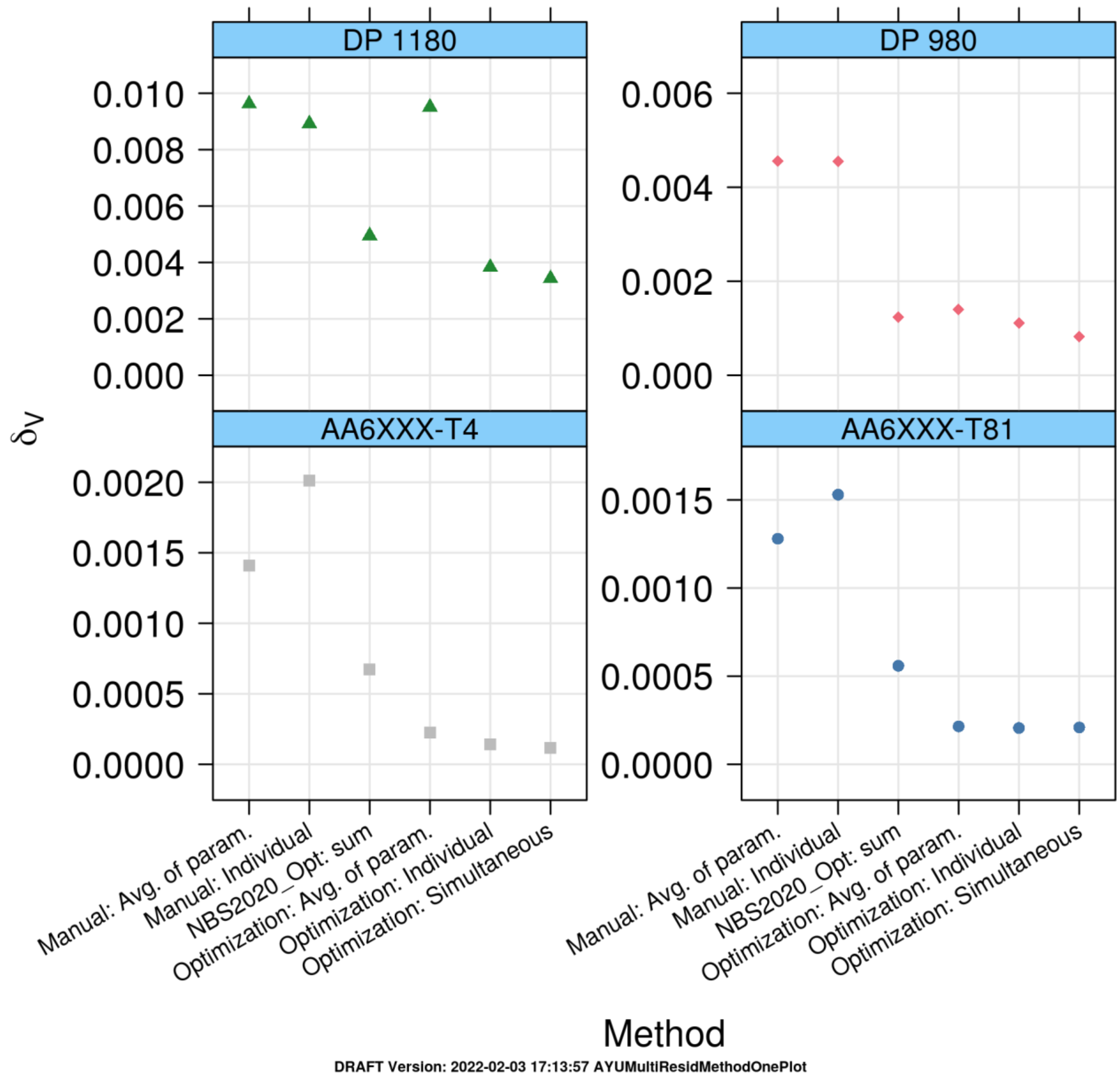

Figure 12 Total residual (normalized), δ_V, for the four alloys, separated by Method and the variant ("Method: variant") used to compute it.

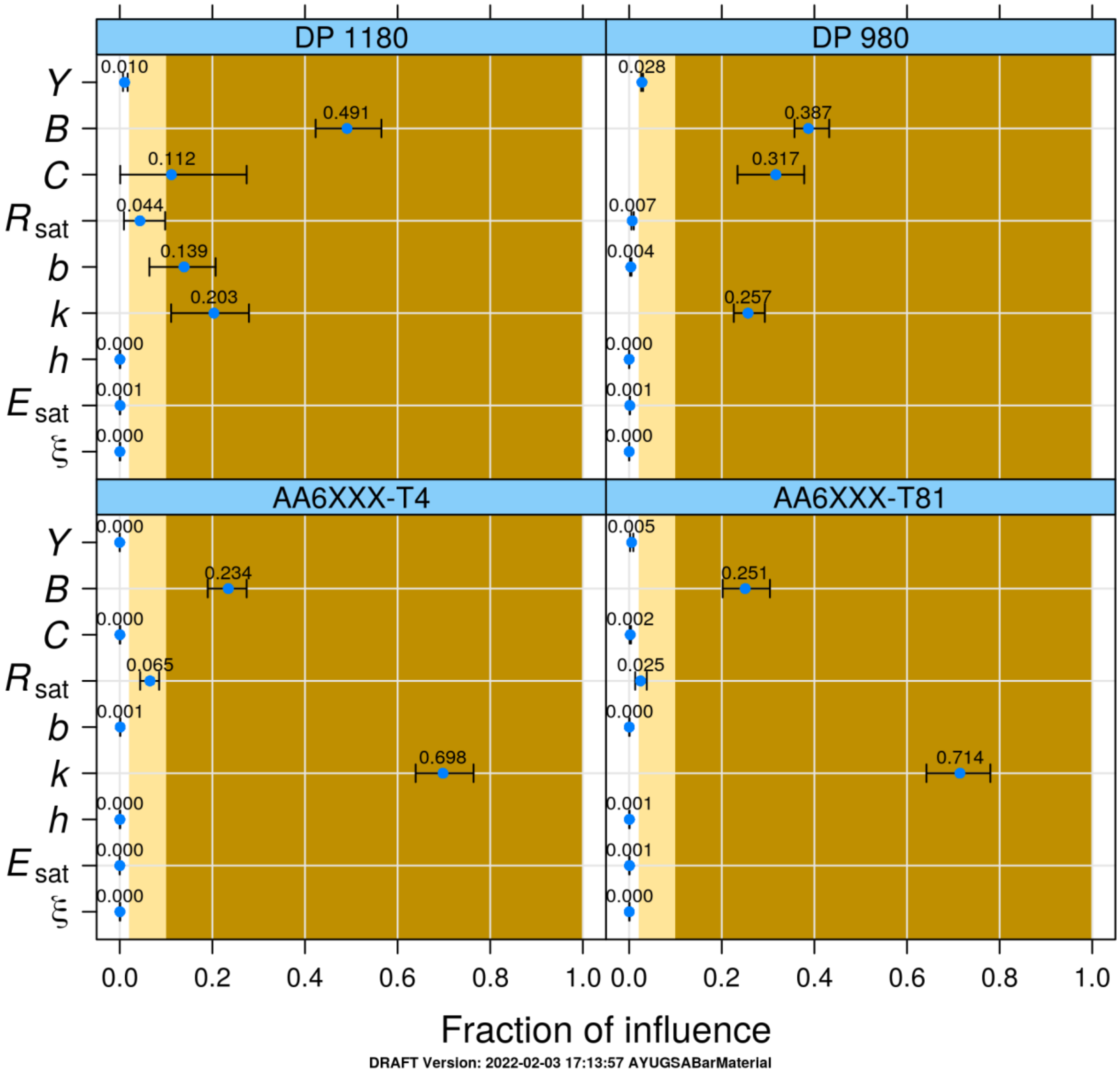

Figure 13 Global sensitivity analysis (GSA). Average (points) and range (bars) for the fraction of influence of each Y-U parameter determined using the Optimization Method. Shading in the body of the plot denotes region of large (dark shading), small (light shading), and no (no shading) influence. Numerical values of the fraction of influence are plotted above the symbol.

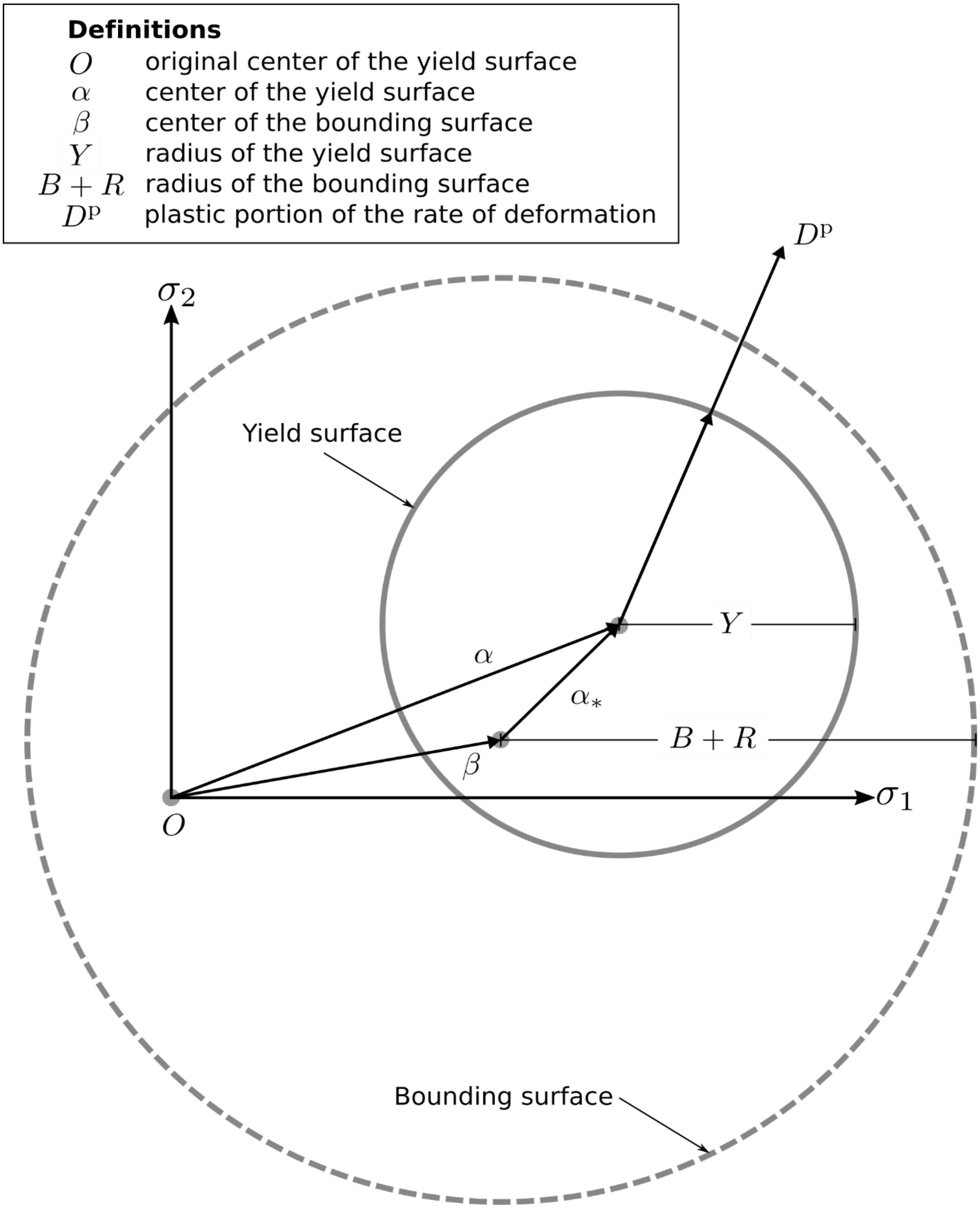

Figure 14 A schematic illustration of the Yoshida-Uemori two-surface model [28].

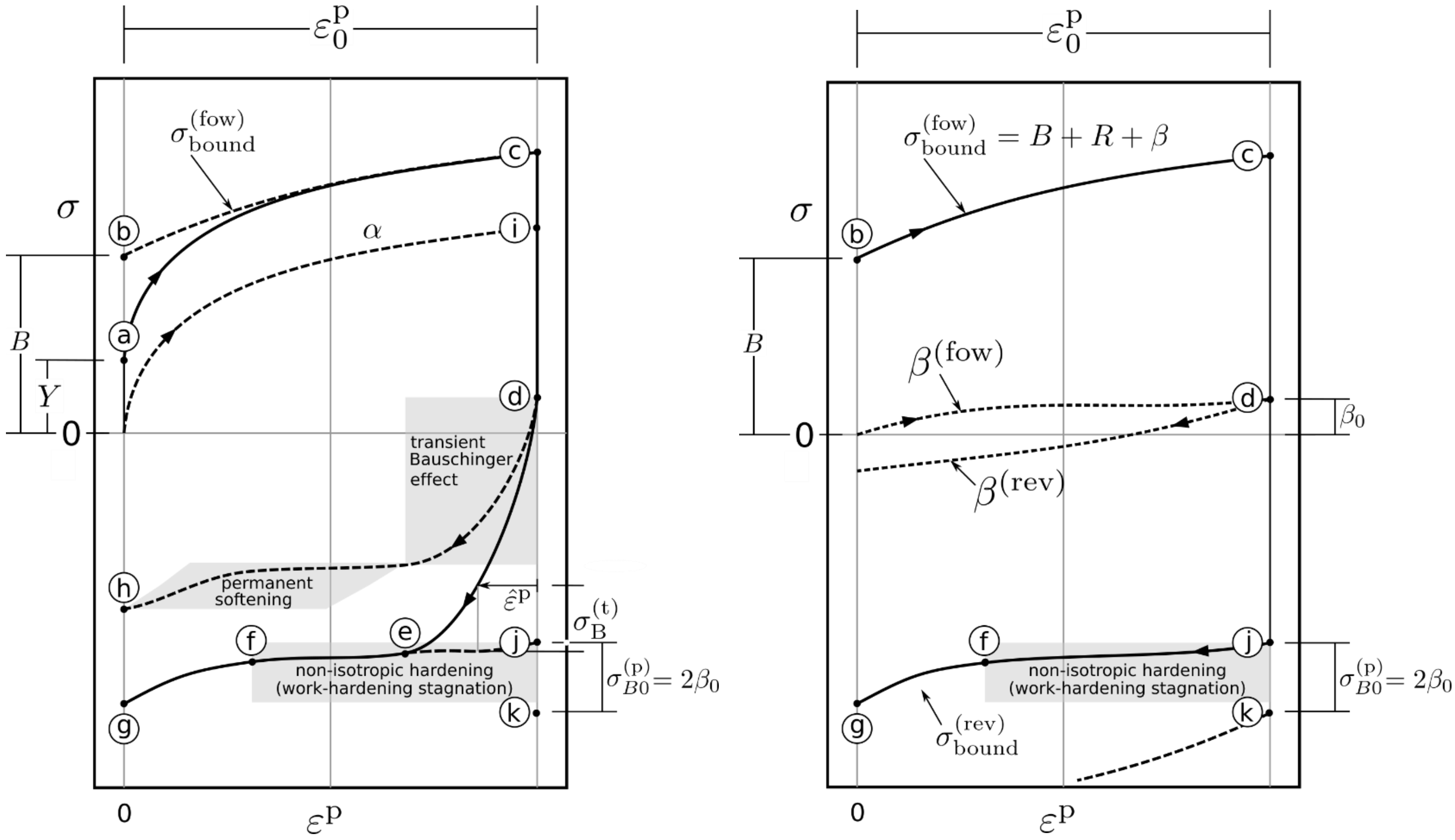

(a)	(b)

Figure 15 A schematic of the changes in the true stress, σ, and true plastic strain, ε^{p}, (a) yield surface and (b) bounding surface (solid lines) during a uniaxial tension-compression test (Y-U).

Table 1 Summary of the ten Y-U parameters.

Symbol	Description	FEA-model designation*
Y	radius of the yield surface	Y
B	initial radius of the bounding surface	CB
C	kinematic-hardening-rate parameter	`SC1, and SC2=0`
R_{sat}	saturated value of the hardening at infinitely large plastic strain	RSAT
b	bounding-surface kinematic-hardening-rate parameter	SB
k	bounding-surface isotropic-hardening-rate exponent	K
h	fraction of hardening that is kinematic, versus isotropic A value of h = 0 signifies fully isotropic hardening, while a value of h = 1 indicates fully kinematic hardening.	H
E_0	Young's modulus at the initial state	E
E_{sat}	Young's modulus at infinitely large pre-strain	ESAT
ξ	Young's modulus degradation rate parameter	COE

* These are the names of the parameters named in the LS-DYNA MAT_125 model [45] *MAT_KINEMATIC_HARDENING_TRANSVERSELY_ANISOTROPIC that this study used.

Table 2 Ranges of Y-U parameters constrained in the Optimization Method.

		AA6XXX-T4		AA6XXX-T81		DP 1180		DP 980	
	units	Min	Max	Min	Max	Min	Max	Min	Max
Y	MPa	100	200	100	300	600	900	500	800
B	MPa	100	300	100	325	500	1300	600	1025
C		250	900	150	900	100	800	115	450
R_{sat}	MPa	80	400	80	325	1	300	100	225
b	MPa	1	50	1	50	80	500	30	110
k		2	50	2	50	1	130	2	75
h		0.05	0.7	0.05	0.7	0.1	0.75	0.3	0.7
E_{sat}	MPa	60000	70000	60000	76000	160000	175000	160000	174000
ξ		80	150	80	200	25	125	25	110

Table 3 Values of ten Y-U parameters for all four materials for all methods.

Method	Variant	Replicate	Y MPa	B MPa	C	R_{sat} MPa	b MPa	k	h	E_0 MPa	E_{sat} MPa	ξ	δ	$δ_V$
AA6XXX-T4														
Manual	Individual	R01	176.8	174.2	419.3	142.7	4.05	18.6	0.5	69160	NA	0	5.798E-04	2.010E-03
Manual	Individual	R02	176.8	173.5	444.2	128.6	7.8	23.2	0.5	69160	NA	0	5.250E-04	NA
Manual	Individual	R03	176.8	174.3	449.9	164.7	6.99	14.9	0.5	69160	NA	0	6.133E-04	NA
Manual	Avg. of param.	NA	176.8	174	437.8	145.3	6.28	18.9	0.5	69160	NA	0	NA	1.410E-03
Optimization	Individual	R01	161.4	181.6	523.2	220.3	26.5	9.3	0.1	69160	66928.2	126.6	3.060E-05	1.410E-04
Optimization	Individual	R02	180.6	185.8	434.8	226.4	21.9	9.2	0.07	69160	64416.8	98.5	2.280E-05	NA
Optimization	Individual	R03	182.1	180.7	500.6	257.5	30.2	7.9	0.08	69160	68380.6	147.1	2.860E-05	NA
Optimization	Avg. of param.	NA	174.7	182.7	486.2	234.7	26.2	8.8	0.07	69160	66575.2	124.1	NA	2.260E-04
Optimization	Simultaneous	NA	151.2	184.8	564.4	286.9	35.3	6.5	0.05	69160	68819.3	150	NA	1.150E-04
NBS2020_Opt	Numisheet2021	NA	113	193	(850, 500)	230	10	7.7	0.12	70000	65000	110	NA	6.750E-04
AA6XXX-T81														
Manual	Individual	R01	260	257.2	215.7	173.8	12.9	9.7	0.5	69100	NA	0	4.782E-04	1.530E-03
Manual	Individual	R02	260	259.3	212.3	174.4	12.6	9.5	0.5	69100	NA	0	4.105E-04	NA
Manual	Individual	R03	260	259.7	289.9	187.4	15.75	8.7	0.5	69100	NA	0	4.606E-04	NA
Manual	Avg. of param.	NA	260	258.7	239.3	178.5	13.75	9.3	0.5	69100	NA	0	NA	1.280E-03
Optimization	Individual	R01	255	260	302.9	219.3	32.7	7.6	0.09	69100	68115.4	125.3	3.350E-05	2.060E-04
Optimization	Individual	R02	251.8	263.3	307.4	285.2	35.5	5.5	0.1	69100	66952.7	150.8	2.340E-05	NA
Optimization	Individual	R03	238	261.7	408.4	256.7	49.9	6.1	0.06	69100	70345.7	180.7	3.230E-05	NA
Optimization	Avg. of param.	NA	248.3	261.7	339.6	253.7	39.4	6.4	0.09	69100	68471.3	152.3	NA	2.150E-04
Optimization	Simultaneous	NA	249.5	261.7	318.7	228.7	28.3	7.3	0.12	69100	68282.3	103.7	NA	2.090E-04
NBS2020_Opt	Numisheet2021	NA	175	267	(900, 450)	190	15	8.5	0.2	72000	68000	150	NA	5.590E-04
DP 980														
Manual	Individual	R01	770	804.6	143.2	186.7	60.99	59.8	0.5	211833	168625	37.046	1.412E-03	4.550E-03
Manual	Individual	R02	770	817.4	156.4	153.02	85.7	56.03	0.5	211833	168625	37.046	1.347E-03	NA
Manual	Individual	R03	770	817.3	159.9	150.2	93.3	57.3	0.5	211833	168625	37.046	1.471E-03	NA
Manual	Avg. of param.	NA	770	813.1	153.2	163.3	80	57.7	0.5	211833	168625	37	NA	4.560E-03
Optimization	Individual	R01	680.6	965.1	125	100	110	12.6	0.7	211833	162118.2	80.9	1.621E-04	1.110E-03
Optimization	Individual	R02	650.9	978	115.6	100	110	9.2	0.5	211833	160000	100.1	1.785E-04	NA
Optimization	Individual	R03	659.4	967.4	115	100	110	11.8	0.69	211833	160000.1	100.2	1.923E-04	NA
Optimization	Avg. of param.	NA	663.6	970.2	118.5	100	110	11.2	0.63	211833	160706.1	93.7	NA	1.400E-03
Optimization	Simultaneous	NA	640.3	990.4	115.4	100	100.9	7.4	0.5	211833	161002	71.9	NA	8.180E-04
NBS2020_Opt	Numisheet2021	NA	590	990	(400, 120)	130	50	10.6	0.5	206000	170000	100	NA	1.240E-03
DP 1180														
Manual	Individual	R01	842	758.7	626.4	-6.9	451.6	118	0.5	203000	168625	37.046	2.245E-03	8.920E-03
Manual	Individual	R02	842	742.1	678.8	28.7	420.1	120	0.5	203000	168625	37.046	3.107E-03	NA
Manual	Individual	R03	842	747.1	633.7	-5.4	451.6	120	0.5	203000	168625	37.046	2.934E-03	NA
Manual	Avg. of param.	NA	842	749.3	646.3	5.5	441.1	119.3	0.5	203000	168625	37	NA	9.620E-03
Optimization	Individual	R01	762.6	1042	100	1	464.1	46	0.32	203000	169074.6	123.9	6.305E-04	3.830E-03
Optimization	Individual	R02	799.8	934.3	100	68.4	500	57.7	0.49	203000	164042.2	105.1	1.145E-03	NA
Optimization	Individual	R03	659.4	967.4	115	100	110	11.8	0.69	203000	160000.1	100.2	1.103E-03	NA
Optimization	Avg. of param.	NA	740.6	981.2	105	56.5	358	38.5	0.5	203000	164372.3	109.7	NA	9.510E-03
Optimization	Simultaneous	NA	763.1	930.1	100	1	500	59.4	0.53	203000	160000	125	NA	3.430E-03
NBS2020_Opt	Numisheet2021	NA	650	1240	(300, 150)	230	100	3	0.2	200000	165000	100	NA	4.950E-03

Notes

NA : not applicable

"Avg. of param." is an abbreviation for the Average of Parameters variant described in 4.1.2.1

The parameters in rows where Variant=Individual were calculated from the individual replicate curves the Manual and Optimization Methods.

Y, B, C, R_{sat}, b, k, h, E_0, E_{sat}, and ξ are defined in Table 1.

Values in parentheses in rows where Method=NBS2020_Opt under heading C are the values of C_1 and C_2 from the NBS2020_Opt Method. See Section 3.1.2 and Section 3.3.

δ: residual (See Section 4.1.2.1) $δ_V$, total residual for the variant calculated from equation 6

Cells shaded in dark gold denote parameters that had large influence determined by the global sensitivity analysis.

Cells shaded in light gold denote parameters that had small influence determined by the global sensitivity analysis.

Color shading is the same as in Figure 13.

Cells boxed in black denote parameters where the optimization reached or nearly reached an optimization limit. (See Table 2.)